

Modes of propagation and deposition of granular flows onto an erodible substrate: experimental, analytical, and numerical study

Abstract An erodible substrate and a sharp slope break affect the dynamics and deposition of long runout landslides. We study the flow evolution of a granular mass (1.5–5.1 l of sand or gravel) released on a bilinear chute, i.e., an incline (between 35 and 66°) followed by a horizontal sector, either sand-free or covered (1–2-cm-thick sand layer). Monitoring the time evolution of the falling mass profiled at 120 Hz, the impact dynamics, erosion of the basal layer, and modes of deposition are studied. The frontal deposition is followed by a backward propagating shock wave at low slope angles (<45°), or by a forward prograding flow at greater angles. Experiments with colored sand layers show a complex sequence of dilation, folding and thrusting within both the collapsing sand flow and the substrate. Experimental results are compared with real rock avalanche data and nearly vertical collapses. The observed increase of the drop height divided by the runout (H/L or Heim's ratio) with both chute slope angle and thickness of the erodible substrate is explained as an effect of vertical momentum loss at the slope break. Data suggest a complex evolution, different from that of a thin flow basal shear flow. To provide an approximate explanation of the dynamics, three analytical models are proposed. Erosion of a 1-cm-thick substrate is equivalent to 8–12 % increase of the apparent friction coefficient. We simulate the deposition and emplacement over an erodible layer with a FEM arbitrary Lagrangian Eulerian code, and find a remarkable similarity with the time evolution observed in the experiments. 2D models evidence the internal deformation with time; 3D models simulate deposition.

Keywords Granular flow · Erosion · Slope break · Physical modeling · Rock avalanche · Numerical modeling

Introduction

Although it is well known that landslides can be strongly controlled in their evolution and final morphology by the characteristics of the ground surface on which motion and deposition occur, i.e., hard rock versus an erodible substrate, field studies and experiments on the effect of an erodible substrate beneath a landslide have been scarce. In fact, the erodible substrate often remains completely covered underneath the landslide mass, which makes a closer examination difficult (Hewitt et al. 2006; von Poschinger and Kippel 2009; Dufresne 2012). In some cases, however, the erodible substrate has been pushed ahead of the landslide, and traces of substrate flow may still be visible (Choffat 1929; Jaboyedoff 2003; Crosta et al. 2008, 2009) and recorded by the deformed sediments piled up in arched ridges and grooves.

Ancient rock avalanches may still show the evidence of having been affected by an erodible substrate (McSaveney et al. 2000). The possibility that such a substrate behaves like a lubricating layer has been invoked to explain the extraordinary mobility of ancient landslides on Earth (e.g., Flims rock avalanche, von

Poschinger and Kippel 2009) and on Mars (Lucchitta 1979; De Blasio 2011a, b).

The substrate can be entrained, dragged, sheared, plowed, bulldozed by the landslide, or may even remain unaffected if the base of the landslide is decoupled from the substrate due to the presence of a basal lubricating layer taking up the shear. Momentum conservation applied to the overall mass (landslide plus entrained material) will cause the landslide to lose speed compared to the case with no entrainment, at least for slopes below critical slope values (ca. 16° according to Farin et al. 2014). So a key question related to the hazard potential of such events is if it will be more dangerous because of the increased volume and mobility or less dangerous because entrainment tends to decrease its speed. The physical processes occurring during erosion and entrainment of an erodible substrate have not, however, been studied systematically.

Numerous experiments have been performed as a small-scale analog for landslides (Denlinger and Iverson 2001; Forterre and Pouliquen 2008; Lacaze et al. 2008; Lajeunesse et al. 2004, 2005; Mangeney et al. 2007, 2010; Crosta et al. 2008, 2013b; Manzella and Labiouse 2008, 2013; Farin et al. 2014). Most experiments are based on the flow of a granular medium along a flume under controlled conditions and involve monitoring of the flow velocity, evolution of the traveling mass, and the examination of final deposit geometry and runout (e.g., Gray et al. 1999; Pudasaini and Hutter 2006). Most experiments are conducted on a 2–3-m-long flume. Some tests on a larger scale show that the results are nearly independent of the size of the experimental apparatus (Okura et al. 2003). Despite the commonness of landslides traveling on antecedent sediment, comparatively few experiments have addressed the problem (Crosta et al. 2008, 2009; Mangeney et al. 2010; Rowley et al. 2011; Dufresne 2012; Farin et al. 2014). Rowley et al. (2011) completed a set of systematic experiments where a released mass of impact beads (also known as ballotini®) interacted with another horizontal layer of ballotini deposited on a 5° slope. They measured comparable runouts when changing the release volume at a fixed slope angle (35°), and observed the formation of inverted stratigraphic structures in the final deposits. These are explained by the authors as Kelvin-Helmoltz instability connected to changes in density and velocity between two granular materials in contact. Mangeney et al. (2010) and Farin et al. (2014) studied experimentally the effect of dry sand lying on a sloping ground on the runout of granular flows. They demonstrated that under different conditions and preparation modes of the basal layer (e.g., degree of compaction), the runout may increase even on a very thin erodible bed. This longer runout is associated with higher flow velocity during the deceleration and slow propagation phases.

In this work, a joint experimental, theoretical, and field analysis work is set up to investigate the effect of an erodible substrate on the motion of a landslide. The process of interaction of a landslide

traveling on an horizontal erodible substrate with a small-scale granular flow released onto a sand layer is simulated in a setting similar to the one adopted by Rowley et al. (2011). The experiments are recorded with high-speed cameras, and the time-dependent evolution of the landslide is measured with precision.

The adopted bilinear slope geometry allows for a more controllable experimental setting, and it is compatible with landslides collapsing onto alluvial plains where an erodible substrate is most likely to be present. This geometry allows also to investigate the influence on the propagation of the granular mass of the presence of an abrupt break of slope. Numerous rock avalanches have spread along simple bilinear profiles (Fig. 1): in Tien Shan Mts. (Strom 2006); the Elm rock avalanche (Heim 1882, 1932; Hsu 1975); the Frank rock avalanche (McConnell and Brock 1904); Las Colinas, El Salvador (Crosta et al. 2005); Arvel, Switzerland (Choffat 1929; Jaboyedoff 2003, and Crosta et al. 2008, 2009); and along many Martian slopes (Lucchitta 1979). The slope geometry, the scar size, and the presence of basal erodible substrate probably did not allow for a steady flow condition to fully develop in all these cases.

Different classes of models (Pastor et al. 2014) have been proposed in the literature to study the runout of fast-moving landslides. Empirical and semi-empirical models are based on direct field observations and easily measurable variables. Okura et al. (2000, 2003) propose an approach based on the energy line method for a sledge-like model in which vertical component of the kinetic energy is lost at the impact occurring when a landslide passes through an abrupt slope change. The same approach was adopted by Crosta (1992) to simulate the loss of energy in similar geometrical conditions or when a rockslide-rockfall impacts at the base of a steep rocky cliff. This approach fits well the loss of mobility (i.e., decrease in runout) in presence of geometrical constraints. Lied and Bakkehoi (1980) proposed a simplified semi-empirical model for snow avalanches ($\alpha\beta$ -model) to predict the runout distance based on distance at which the avalanche path makes an angle of 10° with respect to the horizontal.

Mathematical models include different levels of complexity and adopt different approaches in the solution. Depth-averaged models have been frequently used to simulate long runout granular flows including levee deposition, basal erosion, pore pressure generation, and dissipation (e.g., Iverson 2012; Pastor et al. 2009, 2014; Mangeney et al. 2007). Discrete element method (DEM) models have an enormous potential in the simulation of granular flows even if still prohibitive in simulating extremely large number of particles (Calvetti et al. 2000; Staron 2008; Taboada and Estrada 2009). Models adopting depth-integrated conservation equations, generalized from shallow-water theory, have been improved to include erosion of a basal layer according to simplified or more complex models (e.g., De Blasio et al. 2011; Iverson and Ouyang 2015). DEM models can directly simulate the interaction between the flowing granular mass and the erodible basal layer or intense shearing allowing for the analysis of internal structures (Taboada and Estrada 2009), the estimate of the pressure acting on obstacles (Utili et al. 2015) or the interaction with fluids (Zhao et al. 2015). A third approach is with finite element methods (Chen et al. 2006; Roddeman 2008; Crosta et al. 2009). In this work, observations attained by laboratory-scale physical models (see Crosta et al. 2015a) are used to develop a series of simple analytical models. As a second step, the prediction capabilities of a numerical finite element method with a combined Eulerian-Lagrangian FEM ALE

(finite element method arbitrary Lagrangian-Eulerian) model and elastic-plastic constitutive laws are verified. This yields additional information which cannot be determined directly from the laboratory experiments (e.g., the evolution of internal deformation). Finally, some of the dynamical phenomena associated to the flow evolution and deposition under the effect of an abrupt slope change are addressed by relatively simple analytical models.

Experiments

Experimental setup

Experimental apparatus

The experimental setup consists of two smooth wooden boards (1200-mm long and 600-mm wide): one with adjustable slope angles (30 to 65° , see Fig. 2 for setting and size) is positioned next to a second horizontal board which can be covered with an erodible substrate of dry sand. An angle greater than 65° would result in a nearly head-on impact against the lower sand-covered plate, while a slope of less than 30° is insufficient for flowage. A wooden box (300-mm long, 150-mm wide, and 160-mm high) containing the granular material is fixed at the upper end of the inclined board at a fixed distance from the upper end of the board, ensuring that a descent length of 900 mm is invariable for different experiments. The down-slope end of the box is closed with a mechanical gate whose opening is controlled by two springs to release the material. The gate opening time is much shorter than the collapse time of the granular material, which ensures a negligible bias on release of the material, as checked through multiple testing and high-speed video recording.

The inclined board is connected to a smooth horizontal board which may be sand-free, or covered by an erodible sand layer (Fig. 2) with different thickness (10 to 20 mm). Two plexiglas side boards allow a direct observation of the experiment from the sides but do not cause any lateral confinement of the released sediment volume (i.e., 1.5 to 5.1 l).

Methods

The granular material in the release box and the erodible sand layer were prepared by hand avoiding uneven compaction. Hand pouring (pluviation) was performed to control the fall height of the sand. Leveling of the deposit was checked and completed by dragging a rigid wooden stick running along lateral supports of fixed height (10 and 20 mm). In order to verify material bulk weight and total released mass, the material in both the release box and in the basal layer was weighed (Table 1).

The tests were performed in controlled environmental conditions with constant temperature and relative humidity, and the material was routinely substituted in successive tests.

The mechanical parameters of interest to these experiments (Table 1) have been assessed by three methods:

- (1) Angle of repose—deposition of sand/gravel cones on different roughened surfaces (smooth or sanded wooden boards) and surveying their geometry and inclination using a high-resolution laser scanner;
- (2) Angle of avalanching—inclining a board with a homogeneous sand layer until avalanching was observed;
- (3) Internal friction—by direct shear testing (ASTM D3080 / D3080M-11 2011) of the materials, and by triaxial test results available in the literature about the Hostun sand.

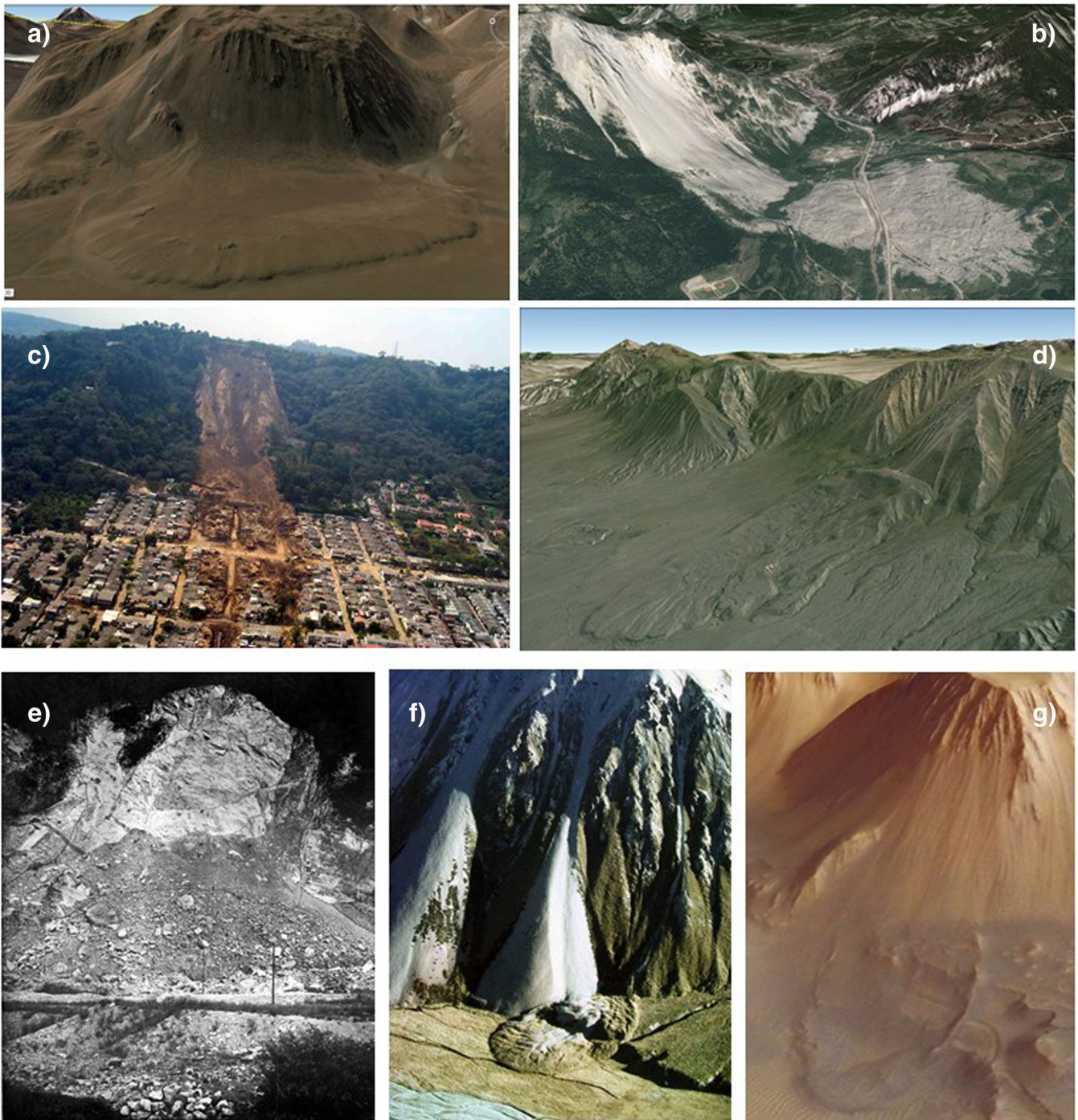


Fig. 1 Example of rock avalanches along simple break of slope profiles and possible interaction with the material at the base of the accumulation. Rock avalanche in Northern Chile (Crosta et al. 2013a) (GoogleEarth™) (a); Frank slide, Alberta, Canada (Cruden and Hungr 1986) (GoogleEarth™) (b); Las Colinas flowslide (San Salvador; Crosta et al. 2005; <http://landslides.usgs.gov/research/other/images>) (c); Central Tien Shan (Strom 2006), rock avalanche in Paleozoic granite (ca $300 \times 10^6 \text{ m}^3$) (GoogleEarth™) (d); Arvel rock fall-avalanche (Choffat 1929) (e); South Ashburton rockslide, New Zealand (McSaveney et al. 2000) (f); Mars, Noctis Labyrinthus (GoogleEarth™) (g). See also Table S1 in supplementary material for geometrical details; a series of typical rock avalanche slope profiles, characterized by a bilinear-like geometry is shown in the figure

To verify the repeatability of the results, a series of preliminary experimental runs were carried out more times in identical conditions for different slope angles, with and without the erodible sand layer on the horizontal board. The fact that the variation in runout was at most of the order $\pm 2 \%$ made us confident on the

statistical soundness of our experimental results. These were followed by a series of tests during which the time evolution of deposition was monitored.

Two high-speed cameras (60 and 600 frames/s) and a laser profilometer (Riegler VZ1000, sampling frequency: 120 Hz; beam

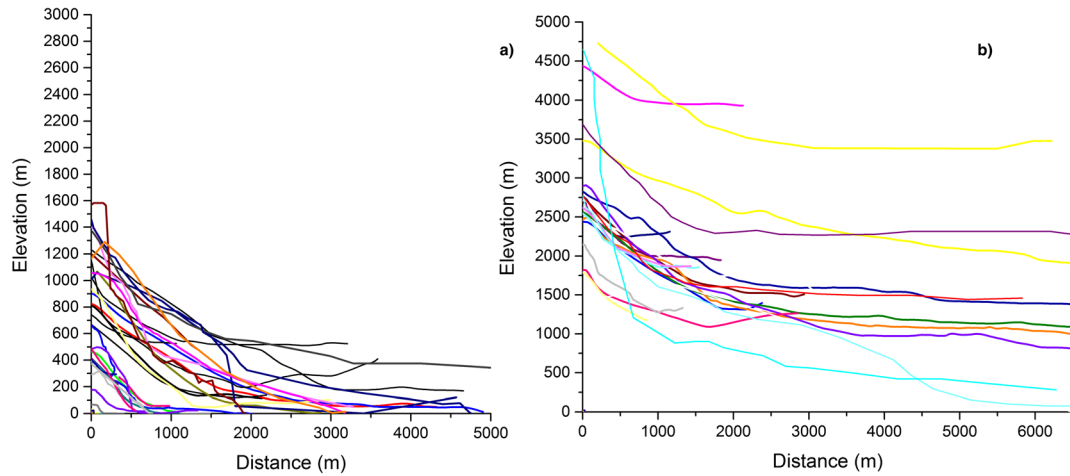


Fig. 1 continued.

diameter: 5 mm; accuracy: 5 mm; and precision: 6 mm, at the test distance ranging between 2 and 4 m) placed in front of the apparatus are used to monitor the flow and capture the landslide evolution in space and time. This allows the propagation velocity of the front to be calculated during different phases of the experiments, which have a total duration of 1 to 1.5 s.

Materials

The materials used in the experiments consist of uniform Hostun silica sand (coefficient of uniformity $D_{60}/D_{10} = C_u = 1.57$; $D_{50} = 0.32$ mm; mean bulk density = 1.42 g/cm³, min bulk density: 1.25 g/cm³; max bulk density: 1.61 g/cm³, according to ASTM D7263-09 2009 particle density = 2.65 g/cm³). This was used for both the released mass and the erodible substrate. In some of the experiments, angular/subangular gravel ($C_u = 1.56$; $D_{50} = 7.5$ mm; mean bulk density = 1.53 g/cm³) was released, keeping the Hostun sand for the erodible substrate. Figure 3 shows the grain size distribution curves of the materials together with main grain size descriptors. In another set of experiments, the same sand on the erodible substrate is colored in stacked layers to explore deformation features associated to the collapse, scraping and thrusting of the erodible substrate. Repeated laboratory testing showed that the colored sand maintained the same physical mechanical characteristics as the ordinary sediment.

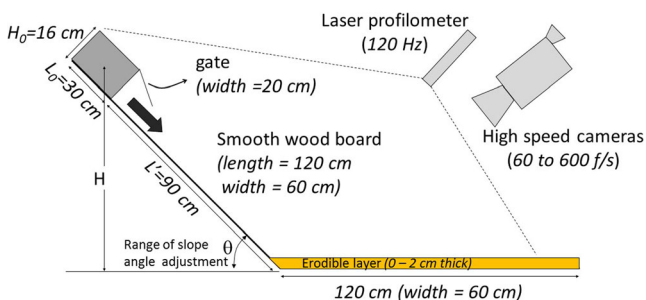


Fig. 2 Sketch of the experimental setup. The time evolution of the flow and the propagation of the front position are observed by sampling the centerline profile at 120 Hz, and by two high-speed cameras

Experimental results

The experimental results and observations are presented for different slope angles and materials (Table 2) in the following order: morphology of the deposit, internal deposit structures, evolution in time of the flow, and deposition along the horizontal board.

Bulk experimental deposit

Figure 4 shows the patterns of experimental deposition for some of the runs with different slope angles (40 , 55 , and 66°), with and without the erodible basal layer, and for different release volumes (1.5 and 5.1 l). These cases have been chosen because they represent well the most important and commonly observed features that will be described in the following. The total runout is found to decrease with the slope angle, whereas the runout along the horizontal part of the path increases. At lower slope angles, a thick bulk deposit forms at the slope break characterized by a series of transversal grooves and furrows. In the case of a smooth surface and high slope angle (Fig. 4g), the tail of the deposit detaches completely from the sloping ground and produces a very elongated apron deposit. The presence of the basal erodible substrate decreases the runout and produces a lunate deposits similar to that of barchans dunes. The proximal deposit (i.e., facing the flow) is steeper, while the distal one is gentler (Fig. 5). A decrease in inclination of the sloping part of the path results in deposits that progressively propagate uphill in a triangular shaped and grooved sedimentation pattern. The inclination of the frontal part of the deposit decreases progressively (22.4 to 14.8°) with the increase in slope angle (e.g., 45 to 60° , see Fig. 5). A much lower inclined front is observed in the case of propagation on a smooth horizontal surface (e.g., 9.8°), whereas the upstream facing side of the deposit is maintained at approximately the same inclination through the various tests (e.g., 16.9 to 17.4° with the erodible substrate and 19.2° on smooth base in Fig. 5). All these values are well below the angle of avalanching as determined by laboratory tests. Furthermore, the smoother superficial morphology of the deposits is well characterized by the slope angle as computed from the slope profile data. For example, in the case of 45° slope with no basal layer, the change in slope angle occurs smoothly along the entire deposit length. Figure 5b evidences the stepped surface geometry of the deposits by a series of peaks in the slope angle values, with

Table 1 Properties of the granular materials used in the experiments as erodible layer or released granular mass. The terms smooth and sandy apply to the conditions of the deposition horizontal surface

Material	Angle of repose (°)		Angle of avalanching (°)		Internal friction angle (°) direct shear test		Mean bulk density (g/cm ³)	Use in the experiments
	Smooth	Sandy	Smooth	Sandy	Peak	Residual		
Hostun sand	31	33	25.4	31.7	37.7	31	1.42 ± 0.1	Erodible layer Granular flow
Gravel	31	34	28.7	33.2	n.d.	n.d.	1.53 ± 0.1	Granular flow

constant spacing and amplitude. When coarse gravel is released instead of Hostun sand, the deposit still grows upslope with decreasing slope angle, resulting in a rough conic geometry with the apex aligned with the deposit centerline (Fig. 6). The deposit length increases slightly with the board slope angle. While at low slope angles, several isolated particles outrun the deposit front, at steeper angles, the interaction with the basal sand layer increases forming a wedge of material pushed or upraised well in front of the coarse material wedge.

Internal structures of the experimental deposit

To visualize the internal geometry of the deposit, in a series of experiments, some colored sand layers were inserted in the basal sand using the pluviation technique described earlier. The layered sequence is formed from the bottom up by the following: a 10-mm-thick lowermost layer of uncolored Hostun sand in contact with the basal board; a 3-mm-thick layer of orange colored Hostun sand; 5 mm of uncolored Hostun sand; and a 3-mm layer of blue colored Hostun sand (Fig. 7). The resulting experimental deposit (Fig. 7a) was wetted to provide the sand with apparent cohesion necessary for cutting sections through it.

Figure 7b–d shows the deposit and some longitudinal and transversal cuts. The orange layer appears doubled in size in sections both parallel and perpendicular to the direction of flow, while the blue layer, which has been sandwiched between the two, increases in thickness and has upper irregular limit. A lack of both colored layers in the upstream side of the deposit confirms the

erosive action played by the granular flow at the slope break. The blue layer is eroded and re-deposited along the basal movement surface. However, the orange layer at the foot of the slope has been stripped and entrained inside the flow, remaining inside the upper cap of the traveling mass and partially inverting the stratigraphic sequence (orange–blue–orange in Fig. 7e). Closer to the centerline, multiple shear planes with associated thrust fold-like features have been observed in the longitudinal cross cuts. Experiments at lower slope angles, in which the granular flow cannot dig deeply enough into the granular bed, do not result in well-developed layer doubling.

Dynamics

For our dynamical studies, we used two high-speed cameras and a laser scanner. Here, we first consider the succession of processes recorded in the experiments (Fig. 8a, b, c); a quantitative analysis of some issues is deferred to later subsections.

Let us first consider the flow of sand without an erodible substrate (Fig. 8a). As soon as the gate is released, sand spreads laterally and longitudinally. After the initial flow along the inclined plate, the front collides with the flat horizontal plate and then travels for some distance. Consequently, as the speed of the front diminishes, the granular flow tail collides against it from behind, and single grains leap into ballistic trajectories. At this stage, a backward propagation of a sand shock wave is observed similar to those described by Pudasaini and Kroner (2008). The rear of the deposit shifts backward and upslope almost linearly with time. In this phase, ramp-like features are created similar to those exhibited by landslides (last four frames in Fig. 8a). These features suggest a progressive backward shifting of the deposit center of mass following the halt of the front.

In the presence of the erodible substrate (Fig. 8b), the dynamics becomes more complicated because the initial impact of the avalanche front on the flat plate results in dilation of the granular eroded mass and a progressive excavation of the erodible substrate down to a certain depth. The consequent entrainment increases the mass of the granular flow and delays the progression of the flow compared to the case of no erodible substrate. In the first images of the sequence, the evolution and rapid spreading of a very shallow wave ahead of the larger and steep breaking wave are visible (see Fig. 8b).

Particles approaching the deposit from behind jump at an angle corresponding to the slope of the deposit. This allows to estimate the distance reached by grains and the projection velocity (see “Analysis of flow dynamics” section). The fountain of launched particles together with the material set into motion has the form of a dense breaking wave traveling along the top of the granular erodible

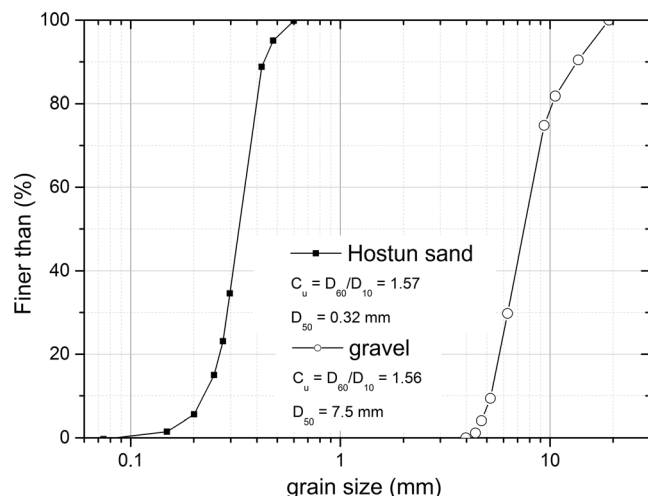


Fig. 3 Grain size curves for the Hostun silica sand and the angular gravel used in the tests. Uniformity coefficient and D_{50} values are also reported

Table 2 Summary of the different test conditions in terms of type of released and substrate material, thickness of the substrate sand layer, volume released, and slope angle

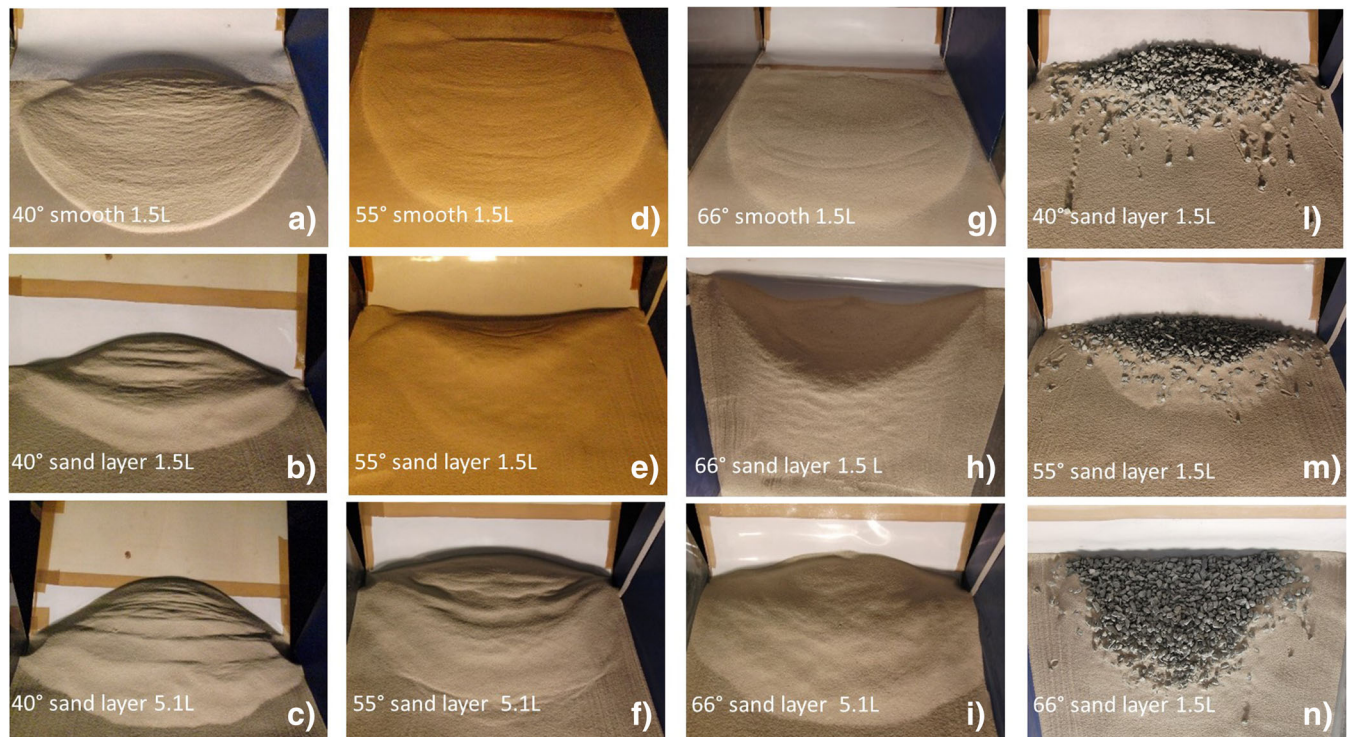
Released material	Substrate	Substrate thickness (cm)	Volume (l)	Slope
Sand	Smooth	0, 1, 2	1.6, 3.4, 5.1	40, 45, 50, 55, 60, 66
Sand	Sand	0, 1, 2	1.6, 3.4, 5.1	40, 45, 50, 55, 60, 66
Gravel	Smooth	0, 1, 2	1.6, 3.4, 5.1	40, 45, 50, 55, 60, 66
Gravel	Sand	0, 1, 2	1.6, 3.4, 5.1	40, 45, 50, 55, 60, 66

substrate. However, as the front builds up, it becomes more dense and massive, and finally stops. In addition, the rear part of the deposit becomes a little bit steeper, which impedes the ballistic jump.

The final geometry resulting from the ramp-like deposition and internal deformation is shown in Fig. 9. Erosion and entrainment make the bulk of the deposit stop earlier; however, the later sequence of processes is similar to the case with no erodible substrate. Figure 8c shows the case for a gravel granular flow. Due to the greater mass of the falling particles, the impact-induced dilation of the sand layer increases, the erosion is deeper, and more material is entrained. Strongly diluted sand of the erodible substrate, set in motion by the incoming gravel, travels ahead of the resulting flow, forming the steep frontal part of the wave and eventually the final deposit, while gravel does not overtake the eroded sand. As the main frontal mass stops, the shock wave propagates upstream in a stepped (ramp-like) mode with a rough pyramidal geometry controlled by the discharge of the flow and volume of the material forming the flow tail.

Accumulation

Based on the analysis of the internal structure observed in tests with colored sand layers and the qualitative analysis of the temporal evolution of the flow and deposition, a three-phase mechanism of flow and deposition is distinguished. In the first phase, the bulk of the granular flow collides with the flat plate. In the second phase, the granular flow causes dilation and erodes the substrate and then leaps in ballistic flight, hitting the top of the deposit with a perturbation in the form of a wave front, which becomes progressively steeper (Fig. 9b) and then gradually loses inclination. In the final stage, and at low slope angles (i.e., $\theta < 40\text{--}45^\circ$), the front of the deposit stops flattening out progressively while the rest of the flow, which is still depositing at the rear of the heap, builds up a series of ramp-like features growing upslope. At higher slope angles, some of the flowing material overpasses the bowed crest of the deposit and generates a gentle leeward side deposit with minor undulations.

**Fig. 4** Examples of different deposit characteristics observed for tests release of different volumes (1.5 to 5.1 l) at changing slope inclination (40, 55, and 66°), on a smooth surface or on a basal sandy layer. a–f Tests with sand. i–n Tests with gravel on sand

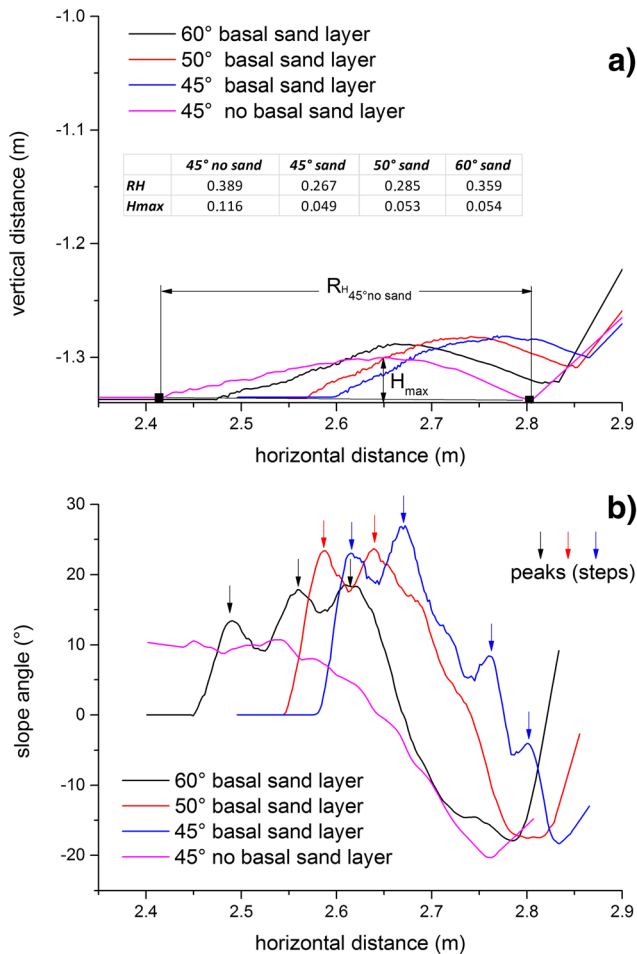


Fig. 5 Comparison of final deposit morphologies at varying slope angle (45 to 60°) and with or without the basal sand layer. Test material: Hostun sand. **a** Deposit profiles as surveyed along the centerline with the axis origin at the position of the laser acquisition system. The inset table shows the values of maximum deposit length (L) and maximum thickness (H_{max}). **b** Slope angle computed on a 10-point smoothing window. *Arrows* evidence the peaks in the slope angles which can be associated to internal deformations and backward propagation of the deposit

To quantitatively analyze this sequence of phases, flow profiles along the model centerline have been monitored at a 120 Hz frequency (at 0.025-s interval, see Fig. 9). For all types of tests (Fig. 9), we observe a change of behavior as a function of the slope angle. At 40° angles, the backward propagating shock wave deposits at a constant rate until exhaustion of the flow. At 45°, the behavior starts changing from a backward to a more downward deposition, and at 50° and then 60°, the rear part of the flow passes over the main mass elongating the deposit (see Fig. 9b, sand on sand layer).

For the gravel on sand layer experiments, Fig. 9c shows that eroded sand is raised and pushed up in front of the falling gravel mass and extends well beyond the tip of the gravel mass, recognizable in the profiles by the very rough surface. Figure 9d, an enlargement of the 45° case in Fig. 9b (with vertical exaggeration) illustrates the progressive formation of the frontal wave, the steepening front, and the successive readjustment of the frontal slope to a gentler angle.

The front velocity reaches a maximum at the beginning of the wave formation and raises again during the readjustment of the front slope angle (up to a final 21.5° value) before the deposit comes to rest. The Froude's number, computed considering the maximum wave height, shows supercritical flow just at the beginning of the propagation along the sub-horizontal part of the path, which becomes rapidly subcritical during most of the spreading and deposition. In contrast to Pudasaini and Kroner (2008), who feed their system with a continuous steady state flow, these experiments are strongly transient (Figs. 9, 10, and 11). The highest observed values of backward accretion velocity ranges between 0.1 and 0.2 m s⁻¹ in our experiments. The interval upon which the shock wave wedge accretes linearly with time is short due to the instantaneous release of the granular medium and the progressive rapid change in sand discharge.

A complete summary of the experimental observations can be attained by plotting the change in elevation along the centerline of the model with time. These spatio-temporal plots provide a clear visualization of the front evolution and of its velocity during the propagation along the horizontal part of the path (Fig. 10). Figure 10 shows three spatial-temporal plots for the case of sand on smooth surface (a), sand on sandy erodible substrate (b), and

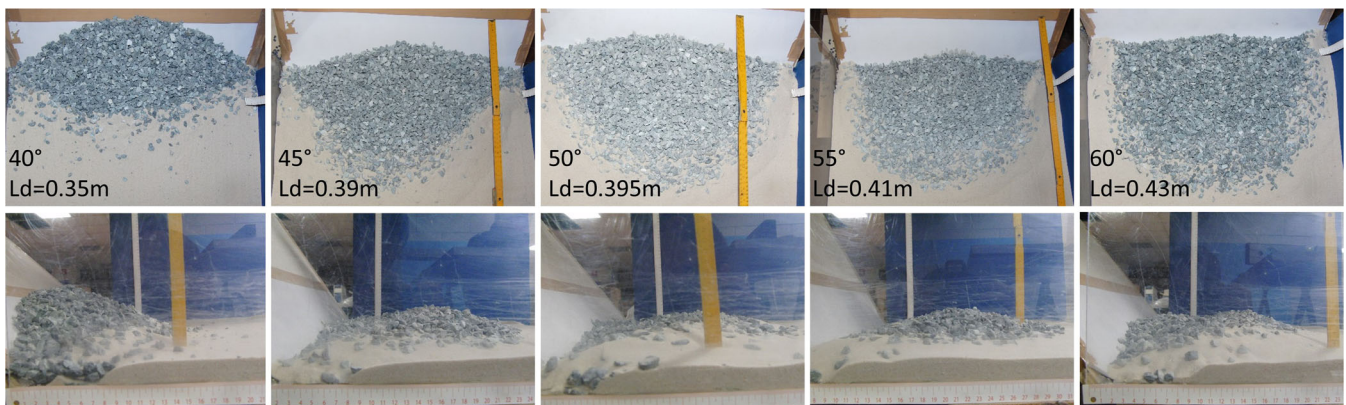


Fig. 6 Final geometry of the deposit of gravel above the basal sandy layer at increasing slope angle and for constant release volume. Particles outrunning the main deposit are visible at low slope angles whereas a wedge of disturbed sand appears in the front of the deposit. R_H in the figures represents the length of the deposit

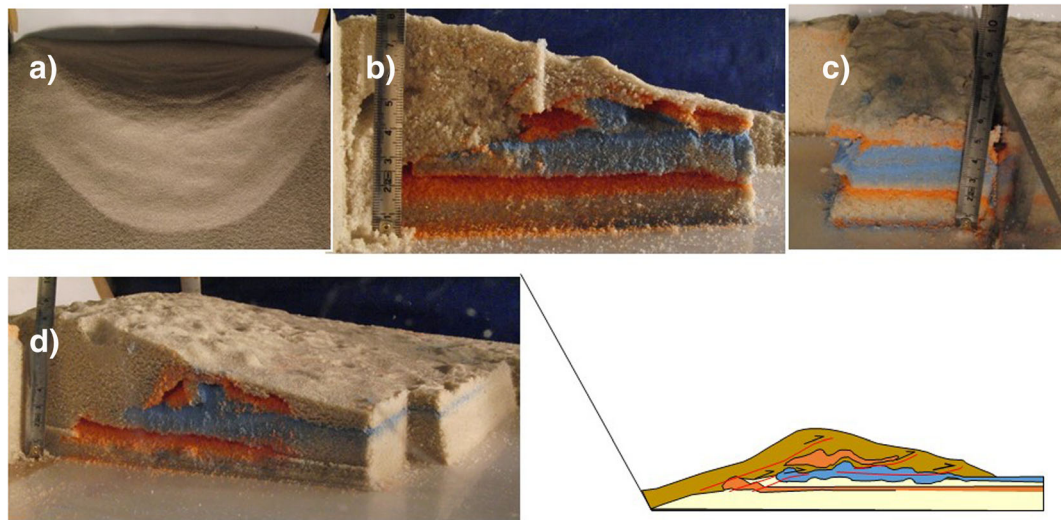


Fig. 7 Internal structures and kinematic interpretation of the erosion and deposition from the result of tests with colored sand layers. **a** Bird's view of the deposit for an experiment with a 66° slope and 5.1 l release volume. **b–d** Longitudinal and transversal sections and view of the deposit. Doubling of the orange layer and thickening of the upper blue layer due to erosion and transport (left to right in **b** and **d**) is visible. The main low angle shearing and erosion plane is seen in **b** by the sharp contact between the uncolored Hostun sand and the colored layers. A simplified description of the general geometry of the layers is shown in **e** where the brownish/mustard tone is used for the granular flow deposit

gravel on sandy erodible substrate (c). On the right hand side of these plots, the sloping plane profile and the disturbance in geometry generated by the descending material are reported. The slope of these curved features yields the velocity of the fronts along the plane and in proximity of the impact at the slope toe. The mean terminal velocity computed for the different experimental conditions is plotted in Fig. 11 against the theoretical friction-free fall velocity $\sqrt{2gL'\sin\vartheta}$ and the velocity with friction $\sqrt{2gL'(\sin\theta - \cos\theta\tan\phi)}$ where ϑ is the slope angle, ϕ is the

friction angle, g is the gravity acceleration, and assuming different values of the basal friction angle, different slope angles, and a constant length of the inclined path $L' = 0.9$ m.

When the avalanche front starts its propagation on the horizontal layer (i.e., at the slope toe where the 0 value of the x axis is fixed), the ballistic launch, initial erosion, and the front wave formations form a cusp which progressively enlarges with time. This cusp becomes more evident with the increase in slope from which the instantaneous velocity of the flow at different elevations (e.g., the base) is obtained.

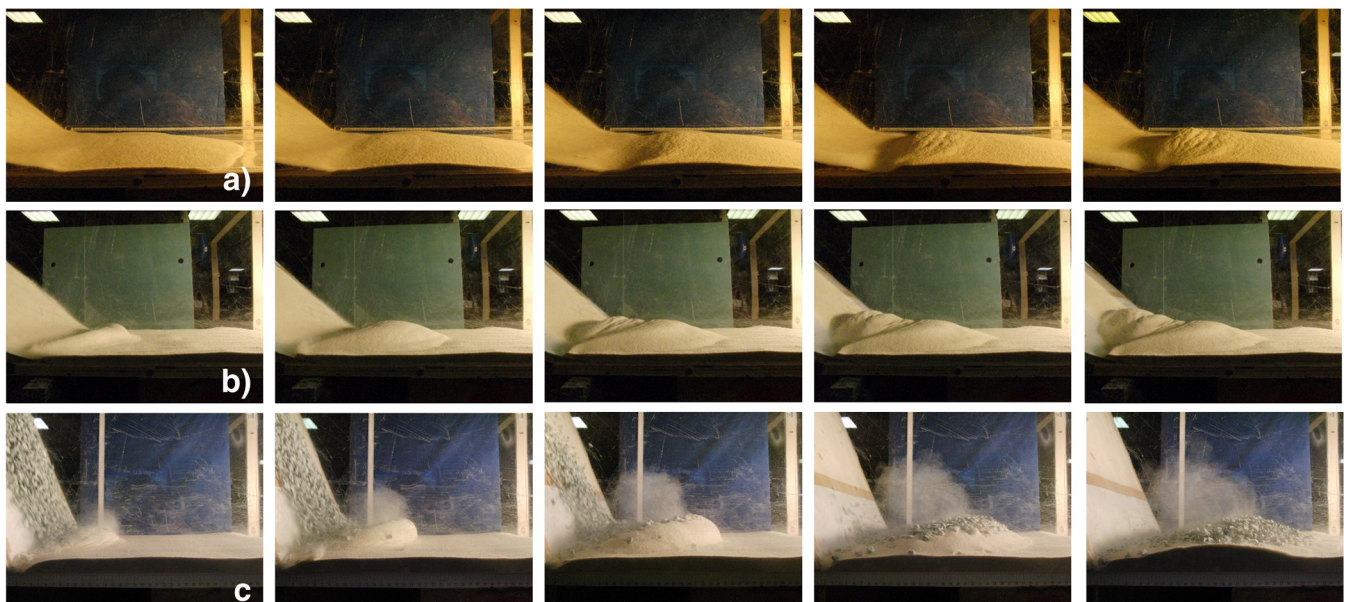


Fig. 8 a Time-lapse sequence of photos showing the evolution of the granular flow for a Hostun sand mass flowing on a 40° slope (a), from the impact on the smooth (rigid) horizontal board to final deposition; for a Hostun sandy mass flowing on a 40° slope (b), and a gravelly mass flowing on a 66° slope (c), both from the impact on the basal layer of the Hostun sand to final deposition. Time runs from left to right and top to bottom images. Time interval: 0.096 s

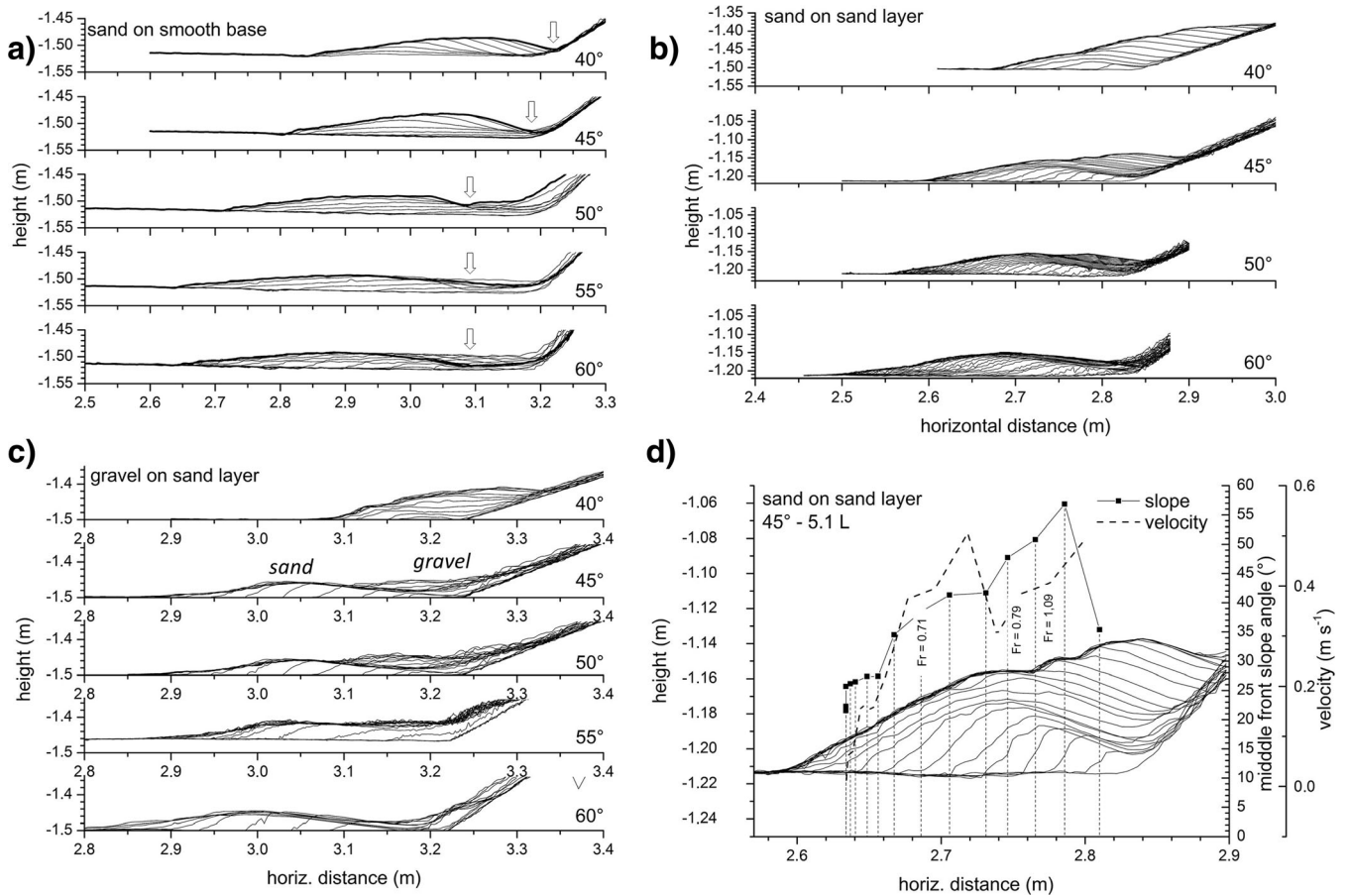


Fig. 9 Evolution of profiles of the flowing mass for different times and different experimental conditions. Each profile portrays the sand distribution every 0.02 s. **a** Sand on a smooth base; *arrows* indicate the farthest point reached by the last grains. **b** Sand on basal sand layer. **c** Gravel on basal sand layer. **d** Enlargement of profiles from **b** for a 45° slope, with computed front slope angle and velocity. Froude number is shown at three different points

In the case of gravel flowing on sand, the propagation of the eroded sand wave in front of the gravel is recognizable by the much smoother surface with respect to that of the gravel material. Starting from these plots, the front position with time has been reconstructed (Fig. 12). Sand avalanches on smooth surface are the most mobile followed by the gravel on sand flows for which sand is mobilized by the falling gravelly mass. Sand is much less mobile when spreading on the sand basal layer. Notice that both for sand

on smooth surface and for gravel on sand, the longest horizontal runout is measured for the steepest slopes, whereas for the sand on sand the maximum spreading is observed at a slope of 55°. This dynamics differs noticeably from the one observed for propagation along constant slope canals. The lower runout for eroding granular flows is reflected in the H/L diagram (Fig. 13). In Fig. 13a, this ratio is shown as a function of the slope angle. Note that data points for the experiments without erodible layer fall below the

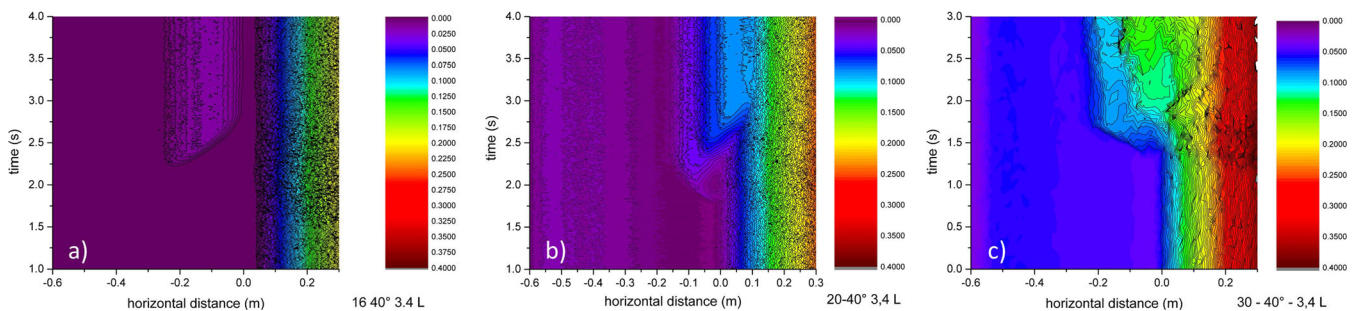


Fig. 10 a Space-time plots showing the evolution with time of the flow profile (z value) along the flow/deposit centerline for a sand mass on smooth surface (**a**), a sand mass on an erodible sand layer (**b**), and a gravel mass on an erodible sand layer (**c**). All the tests are performed releasing 3.4 l of material on a 40° slope. Frequency of acquisition: 120 Hz. Contour interval: 0.005 m. The values reported in the graphs (e.g., 16 40° 3.4 L) refer to the test number, the slope inclination, and the release volume. More results are presented in the Supplementary material (Figs. S1 a, b, c)

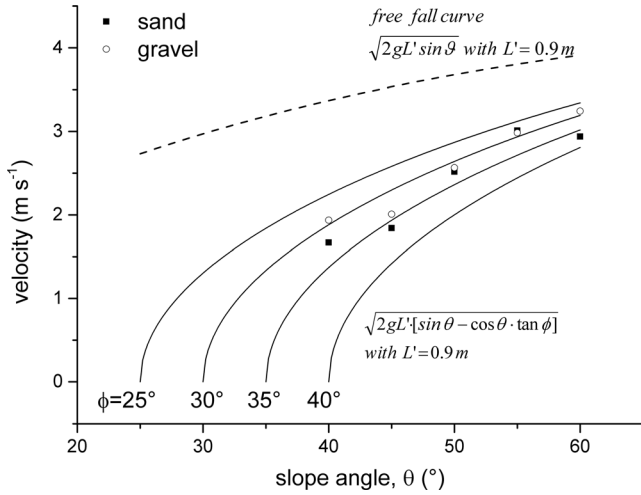


Fig. 11 Final velocity at the end of the sloping board for sand and gravel as derived from monitored profiles, compared with theoretical results for free fall and fall along the slope at constant path length ($L' = 0.9$ m) and changing slope angle (θ), and for variable friction angles ($\sqrt{2gL'(\sin\theta - \cos\theta \cdot \tan\phi)}$).

rest of the other data points. Moreover, the thickness of the erodible substrate directly influences the H/L ratio at different volumes of the granular flow (3.4 l in Fig. 13b and 5.1 l in Fig. 13c).

Analysis of flow dynamics

Mobility

We start the analysis developing a simple analytical solution which describes the runout including the effect of the slope break. A common measure landslide mobility is the tangent of the Fahrboschung (FB), a proxy to the apparent friction coefficient encountered during the flow (Scheidegger 1973). This is the Heim's ratio H/L between the vertical drop (H) and horizontal spread (L) of the landslide (Table 3), calculated adopting as initial point the rear end of the mass prior to failure, and as an end point the tip of the deposit. For an experimental mass, this ratio is close to the friction coefficient of the granular-bed interface (Erismann and Abele 2001) and can be affected by the aspect ratio of the initial granular mass (Lajeunesse et al. 2004, 2005; Lube et al. 2005; Crosta et al. 2009, 2015a). This is because part of the available energy derives from the initial configuration, rather than flowage downslope. For the tests presented in this study, however, this effect should be minimal because the ratio between the vertical size of the containing box and the vertical fall of the center of mass is very small. The relevance of the landslide geometry has been discussed in detail by Lucas et al. (2014) for a constant slope angle (lower than the friction angle), showing the complex dependency of H/L from various variables. Thus, they define a more effective coefficient of friction ($\mu_{\text{eff}} = \tan\theta + H_0/\Delta L$) where the geometry of the initial configuration is accounted for (in our experimental setting a box of length ΔL and thickness H_0). Experiments show a classical relationship between FB and volume, but of limited significance considering the small volumes involved. Moreover, because in these tests the attention was focused on the geometry and characteristics of the flow and deposit along the flat propagation sector (i.e., the valley bottom for many real landslides), the

main goal is the relationship between slope geometry and final runout. The dependence on the characteristics (e.g., roughness and stiffness) surface onto which flow occurs is also of great importance (Crosta et al. 2008).

Figure 14 shows the FB of the experimental granular mass as a function of the different slope angles. In all cases, the FB increases with the slope angle. In the following, we explain this effect noticing that at the break of slope most but not all of the vertical component of the momentum is transferred to the earth surface. If the horizontal component of the momentum is conserved at the slope break, and assuming that this component sums up to a fraction ε of the vertical component of the pre-impact velocity, the absolute value of the velocity past the slope break is:

$$U_x = \sqrt{2gL'(\sin\theta - \mu\cos\theta)} (\cos\theta + \varepsilon\sin\theta) \quad (1)$$

where L' is the length of the sloping board. Technically, ε is a transverse coefficient of restitution, i.e., the ratio between the vertical component of the velocity and the horizontal velocity acquired upon bounce (see Appendix for the list of symbols). This coefficient accounting for the conversion of part of the vertical to horizontal velocity is suggested by the irregularity of geological surfaces, clast shapes, and observed trajectories. This is because the collision of grains against a horizontal and rough surface results in a velocity component parallel to the surface, even when the initial trajectory is perfectly vertical. A grain, even if falling vertically, acquires after bounce a horizontal component owing to the unevenness of both the grain and the table. Obviously, this does not violate momentum conservation, because the extra horizontal momentum acquired by the grain is compensated by an opposite momentum taken up by the Earth. Along a similar line is the model by Okura et al. (2003) based on full loss of the vertical kinetic energy component. The function $\Theta(\theta) = (\cos\theta + \varepsilon\sin\theta)$ in Eq. (1) embodies the effect of the collapse onto the horizontal path. The total horizontal length traveled by the center of mass (first on the inclined board, then on the horizontal portion) is then

$$L = L' \cos\theta + \frac{U_x^2}{2g\mu} \quad (2)$$

and considering that the vertical drop is $H = L'\sin\theta$, substituting U_x from Eq. 1 into Eq. 2, we find a relationship for the ratio between the total drop height and the runout of the kind:

$$\frac{H}{L} = \frac{\tan\theta}{1 + [\cos\theta + \varepsilon\sin\theta]^2 \left(\frac{\tan\theta}{\mu} - 1 \right)} \quad (3)$$

Equation (3) increases monotonically with the slope angle, implying that, the other conditions being equal, a landslide from a steep terrain loses mobility at the slope break compared to one traveling on a smoothly varying terrain. Note that the standard equation $H/L = \mu$ can be retrieved for a unitary value of the function $\Theta(\theta) = 1$ in Eq. (3). It is likely that the coefficient of restitution, considered constant in Eq. (1), will be a function of the angle of impact, increasing for head-on impacts. An alternative choice could thus be $\Theta(\theta) = (\cos\theta + \varepsilon\sin^2\theta)$. Direct calculation shows however only a slight difference in these approaches.

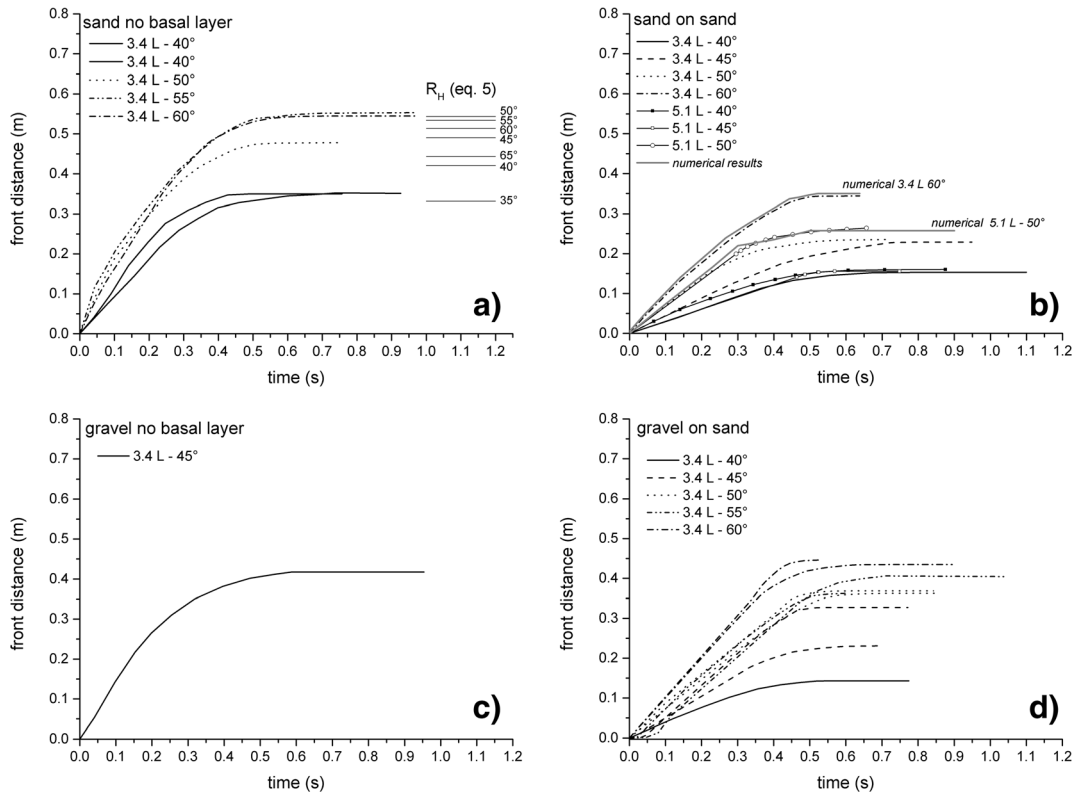


Fig. 12 Front position, along the horizontal sector of the path, versus time plots for different test conditions (volume: 3.4 and 5.1 l). **a** Sand on smooth surface, with comparison of results by applying Eq. 5 for calculation of maximum runout on the horizontal sector. **b** Sand on sand layer, with comparison of results from 3D numerical FEM model (for a 50° slope and 5.1 l and for a 60° and 3.4 l). **c** Gravel on smooth surface. **d** Gravel on sand layer

The fit of the proposed relationship to experimental data is shown in Fig. 14 for experiments on a smooth surface with two different released volumes (3.4 and 5.1 l). The fact that the granular material enters the flume with non-zero velocity can be accounted for by substituting the denominator of Eq. (3) with

$$1 + [\cos\theta + \varepsilon \sin\theta]^2 \left(\frac{\tan\theta}{\mu} - 1 \right) + \frac{B}{\cos\theta L'} \quad (4)$$

where B is the height of the released mass along the vertical direction. Because in our experiments the ratio $\frac{B}{\cos\theta L'}$ is at most 0.15, we neglect its effect.

Starting from Eq. 3, the runout on the horizontal board can be calculated as:

$$R_H = \frac{L' \sin^3\theta}{\mu} \left[\left(1 - \frac{\mu}{\tan\theta} \right) \left(\frac{1}{\tan\theta} + \varepsilon \right)^2 \right] \quad (5)$$

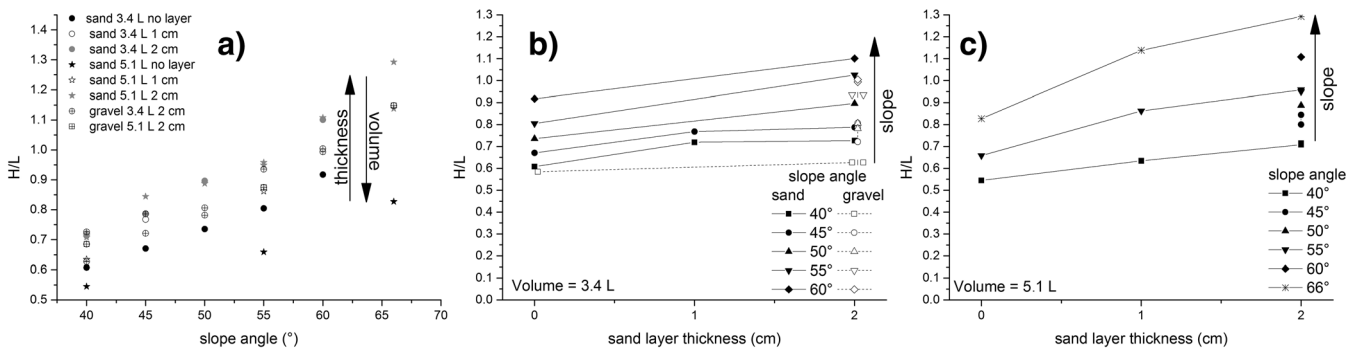


Fig. 13 Drop height/maximum runout length ratio (Fahrboschung) plotted with respect to the slope angle (**a**) for the three different experimental conditions. This relationship also accounts for the fact that for constructional constraints, a greater slope also implies a higher drop height. **b** and **c** The sand layer thickness for different released volumes and materials; sand and gravel (**b**), and only sand (**c**)

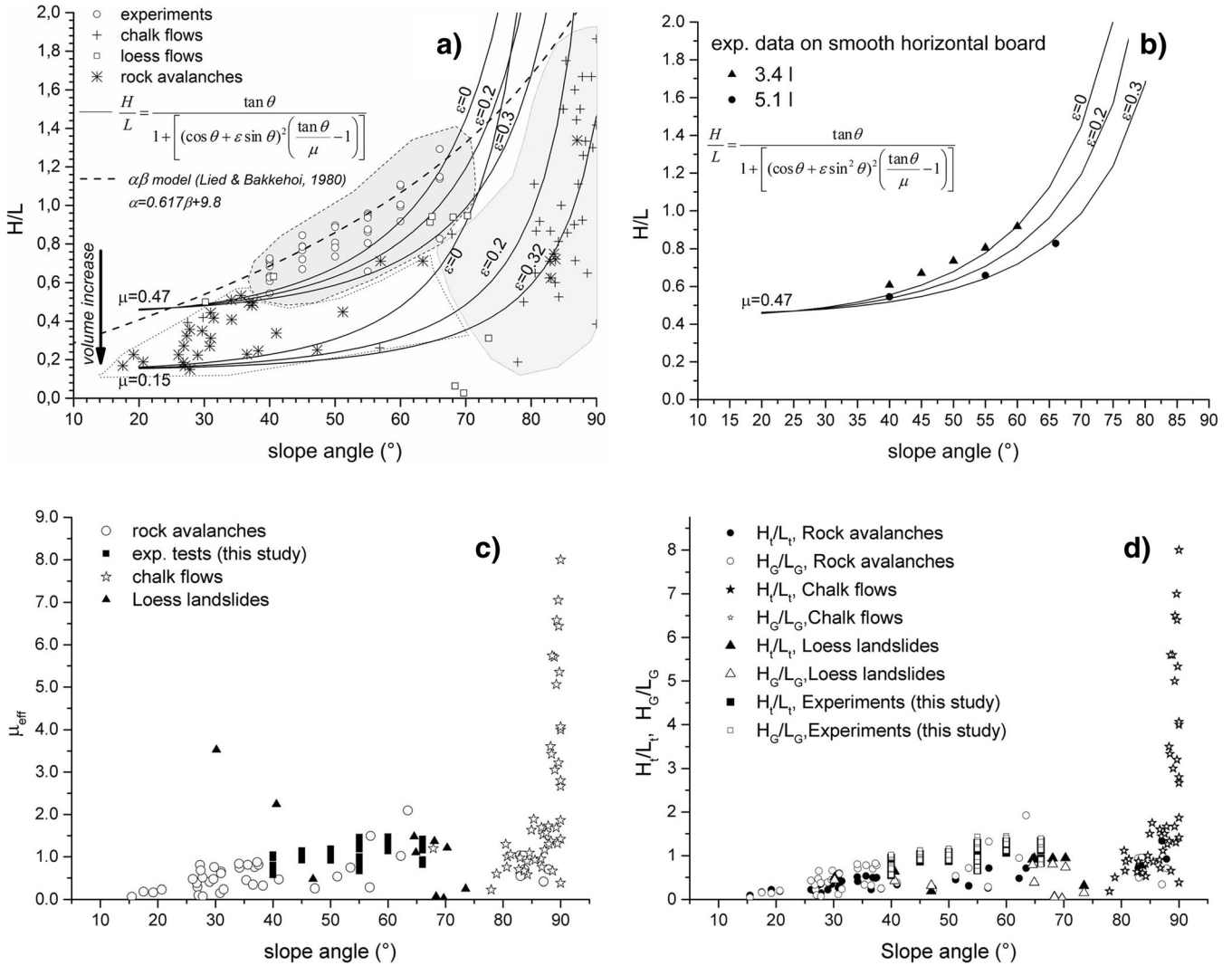


Fig. 14 Figure 9 a Results of the experiments (*circles*) together with data for real rock avalanches (*stars*, see Table S1 in Supporting Information) and chalk falls and flows on tidal flat (*crosses*, from Hutchinson 2002; Duperré et al. 2006) and loess flowslides (Ma et al. 2014). The trend of the predictions of Eq. 1 with the indicated values of ε and μ are also reported. The case of $\varepsilon = 0$ corresponds to the case by Okura et al. (2000). The *thick black line* is the prediction of the $\alpha\beta$ -model by Lied and Bakkehoi (1980) with K and B as in the legend. **b** H/L versus slope angle data for experiments with Hostun sand propagating on an inclined slope and depositing on a smooth (i.e., with no erodible layer) horizontal sector for two volumes of experimental sand (3.4 and 5.1 l). Curves obtained by applying Eq. (3) for a fixed coefficient of friction and three different restitution coefficients are plotted. **c** Results plotted in a larger scale for the effective friction coefficient as defined by Lucas et al. (2014). **d** The same ratio as in **a** but for the center of mass (H_G/L_G) in addition to the previous data

which is a convex function of the angle θ . It initially increases for angles slightly greater than the friction angle and then decreases reaching a minimum value equal to $L'\varepsilon^2/l$. The horizontal runout calculated with Eq. (5) is compared to experimental results in Fig. 15 for propagation on a smooth surface. Even though the values are not exactly the same, Eq. (5) captures the general trend with a maximum runout on the horizontal surface at about 50° . Clearly, the model is not meant to provide a detailed solution as it does not include a volume effect and it refers to the center of mass whereas the experimental data refer to the deposit front.

Apparent friction in presence of an erodible layer

To clarify the increase of apparent friction coefficient in the presence of the erodible medium, we now introduce a simple model based on the momentum conservation. Let the acceleration of the

center of mass of the granular mass along the ramp be described with a friction coefficient $\mu = \tan\phi$ in the form

$$\frac{du}{dt} = g(\sin\theta - \mu\cos\theta) \tag{6}$$

The flow reaches the slope break with a velocity:

$$u_o = \sqrt{2gL'(\sin\theta - \mu\cos\theta)} \tag{7}$$

In the absence of the erodible substrate (i.e., smooth surface), the velocity as a function of the position x along the horizontal board would be

$$u = \sqrt{u_o^2\cos^2\theta - 2gx\mu} \tag{8}$$

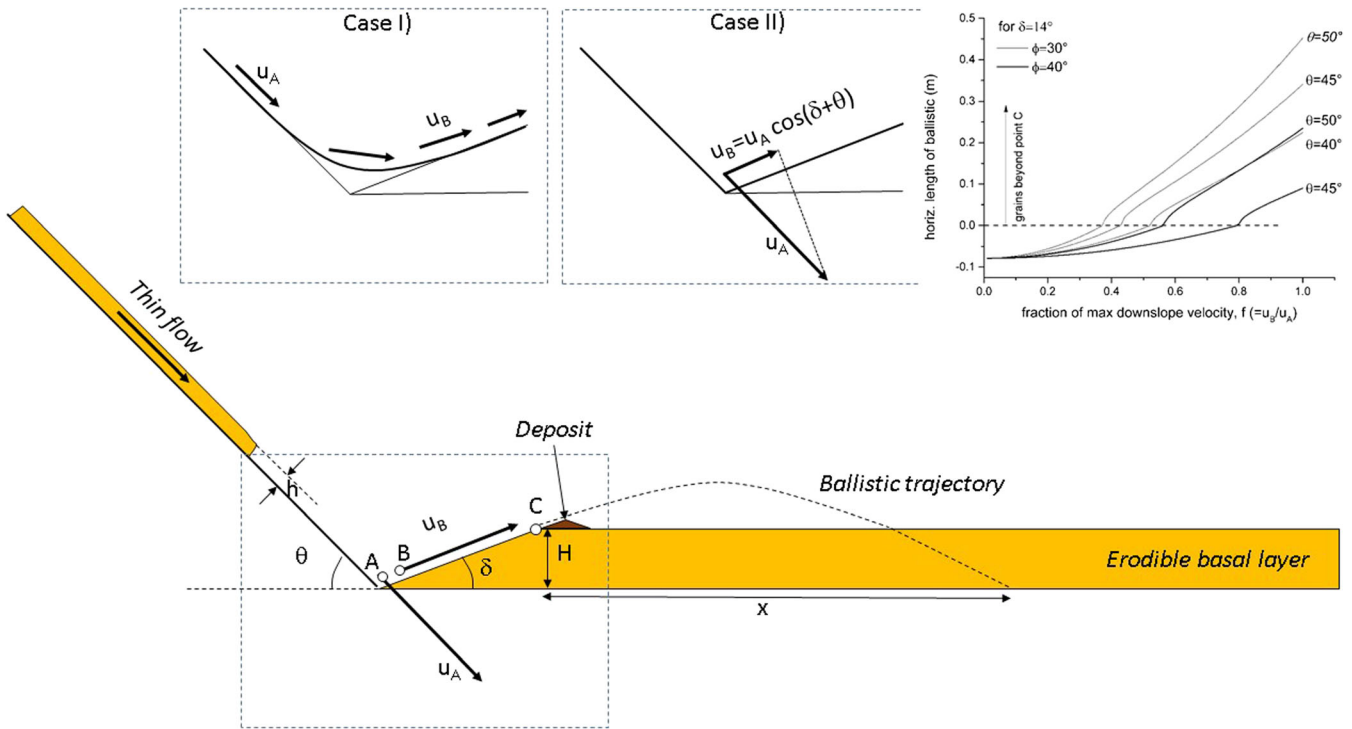


Fig. 15 Geometrical conditions and possible cases for the calculation of the ballistic generation of the frontal wave. In contrast with other experimental and real conditions with fixed angle δ , in these experiments, δ can change according to the erosion by and deposition of the flowing material. *Case I* Entry velocity fully preserved during the change in direction. *Case II* Exit velocity equal to the component parallel to the ramp excavated in the basal erodible layer by the flow. In both cases, the initial velocity for ballistic trajectory results from upslope rise and friction action. *Inset plot in the upper right corner* represents the horizontal length of the ballistic trajectory at varying f for different values of ϕ (30–40°) and θ (40–50°) and a constant δ (14°). *Dashed horizontal line* represents the limit condition beyond which particles can fly ballistic beyond point C

In the presence of the substrate, the granular mass entrains part of the erodible layer down to a depth D' . We assume that the areal extent and the density of the eroded layer are the same as the case of the granular flow. Thus, the momentum $M u_o$ of the granular flow of mass M just before entrainment will be shared between the mass itself and the entrained mass, so that the momentum after entrainment is $[u_{entr}(M + M')]$, where u_{entr} is the velocity after entrainment

$$u_{entr}(M + M') = M u_o \cos \theta \quad (9)$$

and

$$M = S D \rho; M' = S D' \rho \quad (10)$$

where S is the basal surface area of the flow, ρ the density of the granular material, D is the flow thickness before entrainment, M' is the entrained mass of thickness D' . Thus, in the presence of an erodible layer, the velocity as a function of the position is given by

$$u = \sqrt{u_{entr}^2 - 2gx\mu}. \quad (11)$$

We find the horizontal spread, R_{H}^* , of the mass on the flat table in the presence of the erodible layer by putting the argument of Eq. (11) to zero, and using Eqs. (9) and (10). We find that the horizontal spread is diminished with respect

to the case of no sublayer (Eq. 5, assuming a restitution coefficient equal to 0) and is given as $R_{H}^* = R_H / (1 + D'/D)^2$. This results in a Heim's ratio H/L equal to

$$\frac{H}{L}(D') = \frac{H}{L}(D' = 0) \frac{R_H + L' \cos \theta}{R_H + L' \cos \theta} = \left[1 + \frac{2 \cos^2 \theta}{\mu} (\sin \theta - \cos \theta) \frac{D'}{D} \right] \quad (12)$$

In the above equations, the total runouts in the presence and absence of the erodible layer are $R_H^* + L' \cos \theta$ and $R_H + L' \cos \theta$, respectively, while the vertical drop, which disappears from the final expressions in (8), is evidently the same for both cases and equal to $L' \sin \theta$.

Numerically, it is found that 1 cm of erodible material results in 8–12 % increase of the apparent friction coefficient in our experiments. This implies that if the ratio H/L without erodible bed coincides with the friction coefficient (as it ought to), or about 0.58 corresponding to an angle $\tan^{-1}(H/L) = 30^\circ$ (see Table 1), 1-cm-thick erodible layer increases the ratio and the corresponding angle to about 32 and 32.6° at slope angles of 40 and 50°, respectively, which may explain the results observed in Fig. 13.

Note that the apparent friction coefficient appears to saturate as a function of the erodible layer thickness, which indicates a limit D_{MAX} in the depth of granular material that the flow can entrain. This is as also suggested, for different experimental conditions, by Mangeney et al. (2010) and Farin et al. (2014). Thus, if the

thickness of the erodible layer D is less than D_{MAX} , the granular flow will tend to erode the whole layer (weathering limited condition). However, if $D > D_{MAX}$ (transport limited condition), only the part of the erodible layer at depth less than D_{MAX} will be eroded and entrained, which limits the friction angle. The existence of a maximum thickness D_{MAX} is reasonable considering that the shear stress necessary to mobilize a granular material increases with the overburden pressure. Although this estimate, given its intrinsic simplifications, cannot be pushed to any better precision, it is clear that momentum conservation during entrainment can account for much of the observed apparent increase of the friction angle as a function of the erodible layer thickness.

Grains in ballistic flight

The flow of grains hitting the rear of the frontal portion of the deposit and jumping in ballistic flight can be analyzed considering the simple kinematic problem illustrated in Fig. 15. The launch velocity will be controlled by the efficiency of the reflection and the friction force mobilized along the ramp. We assume that the rear part of the horizontal sand layer (i.e., close to slope toe) behaves initially as a “reflecting” surface, and after some erosion has taken place, this develops into a natural ramp from which grains may leap. Two extreme cases can be considered. In the first case, the magnitude of the incoming velocity of grains (u_A in Fig. 15) is preserved after collision (u_B) so that only the direction of the velocity vector is changed. At the other extreme, it is assumed that the component of the velocity of the incoming grain perpendicular to the natural ramp is absorbed by the sand layer, i.e., the normal coefficient of restitution is zero, while the component parallel to the ramp keeps the same velocity corresponding to parallel coefficient of restitution equal to one. In general, the velocity of the grains in position B will thus be a fraction f of the velocity in A , i.e., $u_B = f u_A$. The cases $f=1$ and $f=\cos(\delta + \theta)$ correspond to the first and second state, respectively. They are two extreme cases, and it is to be expected that f should fall between these two extremes. The grain then decelerates as it travels against gravity and friction along the natural ramp of height H from which it leaps in ballistic flight (Fig. 15). The inset plot in Fig. 15 shows the total length of ballistic jumps as a function of the coefficient f calculated with elementary kinematics. Note the threshold behavior as a function of the coefficient and the change in ramp length (up to 0.16 m for this example). If $f < f_{CRIT}$, where f_{CRIT} is a critical value of f (as an example, f_{CRIT} is about 0.37 for the case $\delta = 14^\circ$; $\theta = 50^\circ$; and friction angle 30° illustrated in Fig. 15), the grain has not enough energy to climb up the ramp formed by erosion of the basal layer or piling up of the flowing material. It therefore stops at the rear end of the deposit or erosion groove, in a mode similar to the backward propagating shock wave contributing to building up the deposit. If $f > f_{CRIT}$, the grain has enough energy to rise up the ramp and jump in ballistic flight. Observations suggest a jump distance of the order 80–100 mm, which would correspond to a coefficient f of the order 0.4–0.8.

Verification of the simple model can be achieved by examining the evolution of the backward propagating shock wave. In this phase, the material descending along the slope reaches a velocity controlled by the slope length and inclination, and the coefficient of friction. The velocity after the change in direction (i.e., during the run up along the uphill side of the deposit) is too low, and the flow cannot pass the crest of the deposit. The fact that the granular

material at low slope angles preferentially accumulates at the rear of the deposit can be understood based on simple dynamic considerations. For the granular flow coming from behind, a certain amount of energy is necessary to overcome the deposit. Calling X the maximum horizontal distance reached by the granular flow on the deposit, it follows that

$$f = \left[\frac{2g(\tan\delta + \mu)X}{u_0^2} \right]^{1/2} \quad (13)$$

Because we observe that the X is close to the horizontal length of the upstream side of the deposit, we can compute the value of f during the backward shockwave propagation. In the case of a 45° slope, this gives an experimental slope angle $\delta = 14^\circ$ for the upstream side of the deposit, with an horizontal length $X \approx 9$ cm, a value of f of about 0.8. Again, this value confirms the ballistic jump length observed.

Hakonardottir et al. (2003a, b) carried out a series of experiments where a granular flow of constant depth collided against a dam of given height and inclination angle. They found that when the depth of flow is much less than the dam height, the granular flow upon impact with the dam leaps ballistically with a launch angle equal to the upstream angle of inclination of the dam. This parallels the experimental situation presented here where the dam is substituted by the deposit, whose upstream side is constantly changing shape.

Numerical modeling

Numerical models can support the understanding of granular flow evolution both in time and space, and validate the interpretation given for some of the features observed during the experiments. At the same time, they can test some of the assumptions made about the material behavior. No numerical model results concerning the simulation of such type of processes have been published until now, and this motivates the presented set of simulations.

Numerical method

Because of the large displacements and deformations occurring within a flowing granular material, a Lagrangian finite element method would be subjected to high mesh distortion and inaccuracy. Following previous experience in simulating both small- (Crosta et al. 2008, 2009, 2013b, 2015a) and large-scale granular flows (Crosta et al. 2005, 2006, 2008, 2013a, 2015b) with different characteristics, the same FEM numerical approach (Roddeman 2008; Crosta et al. 2009, 2015a, b;) will be used here. The numerical approach is a combined Eulerian-Lagrangian scheme which demonstrated to provide accurate results under various modeling conditions (Crosta et al. 2009, 2015a, b). We assume an elastoplastic behavior with a standard Mohr-Coulomb yield law, which requires a relatively simple material description. Considering the evidence of a dense flow along the horizontal runout zone (Rowley et al. 2011; Crosta et al. 2015a), this seems a reasonable assumption to be tested through the numerical models. To minimize computational effort, we take advantage of the test symmetry with respect to the centerline and model only half of the chute. The released mass (5.1 l) and the erodible layer (2-cm thick) are assigned the same properties through both 2D and 3D simulations, with an

internal friction of 28.5° , no cohesion, and dilatancy whereas a friction angle of 22° and no cohesion have been assumed at the interface between the granular medium and the smooth surface. These values are derived from the low side of the experimental tests considering also the possible variability of the internal friction angle during motion and deposition. The adopted isoparametric finite elements are 3-noded triangles in two dimensional simulations and eight-noded hexahedrals in three dimensions.

Boundary and initial conditions are coincident with the experimental ones in terms of lateral confinement and release mode. The initial equilibrium stress state for the granular mass contained in the releasing box is reached through quasi-static time stepping so that no inertial effect is introduced. Then gravity is incrementally applied in successive time steps. The release is simulated by deleting a retaining wall. The dynamic equilibrium equations (Crosta et al. 2009) are then solved for the entire area of the spreading material and without introducing pre-imposed controlling conditions both for the onset and the evolution of the material

erosion and deposition. In the following, two sets of results from the simulations are presented, referring to three dimensional (50° slope, 5.1 l and 60° , 3.4 l) and two dimensional experimental layout (66° slope, 5.1 l). This last was performed on a geometry similar to the experimental one, where thin-colored layers were inserted within the erodible layer. For the calculations, 60,814 triangular elements (max size 0.003 m) and 270,380 hexahedral elements ($dz = 0.0025$ m, $dy = dx = 0.01$ m; 10,210 and 19,410 elements for the landslide and the erodible layer, respectively) were used to discretize space in two dimensional and three dimensional simulations, respectively. The different finite elements size is the result of a compromise between resolution of the models and computing time.

Numerical results

Three dimensional simulations (Figs. 16 and 17) show the formation of a large snout, its propagation along the slope and successive impact, erosion, and deposition phases. After the release of the confining wall, the material starts to flow developing a steep

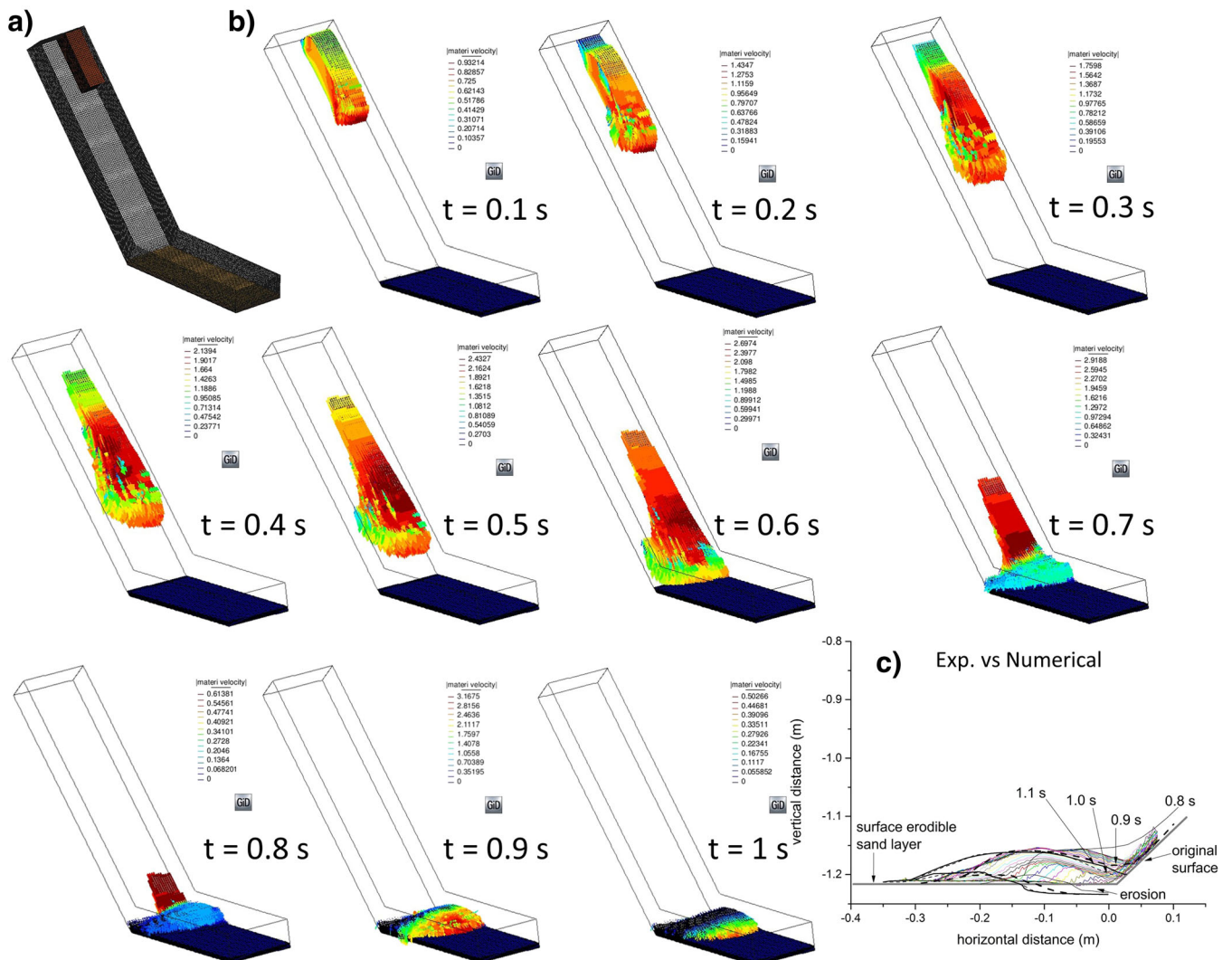


Fig. 16 Three dimensional simulation for a test along a 50° slope, with 5.1 l of sand and a 2-cm-thick basal layer (see also Fig. 15a–S1c). **a** Space discretization. **b** Velocity vectors with colors scaled for each time step. **c** Material and erosion interface profiles at different time steps compared to the experiment

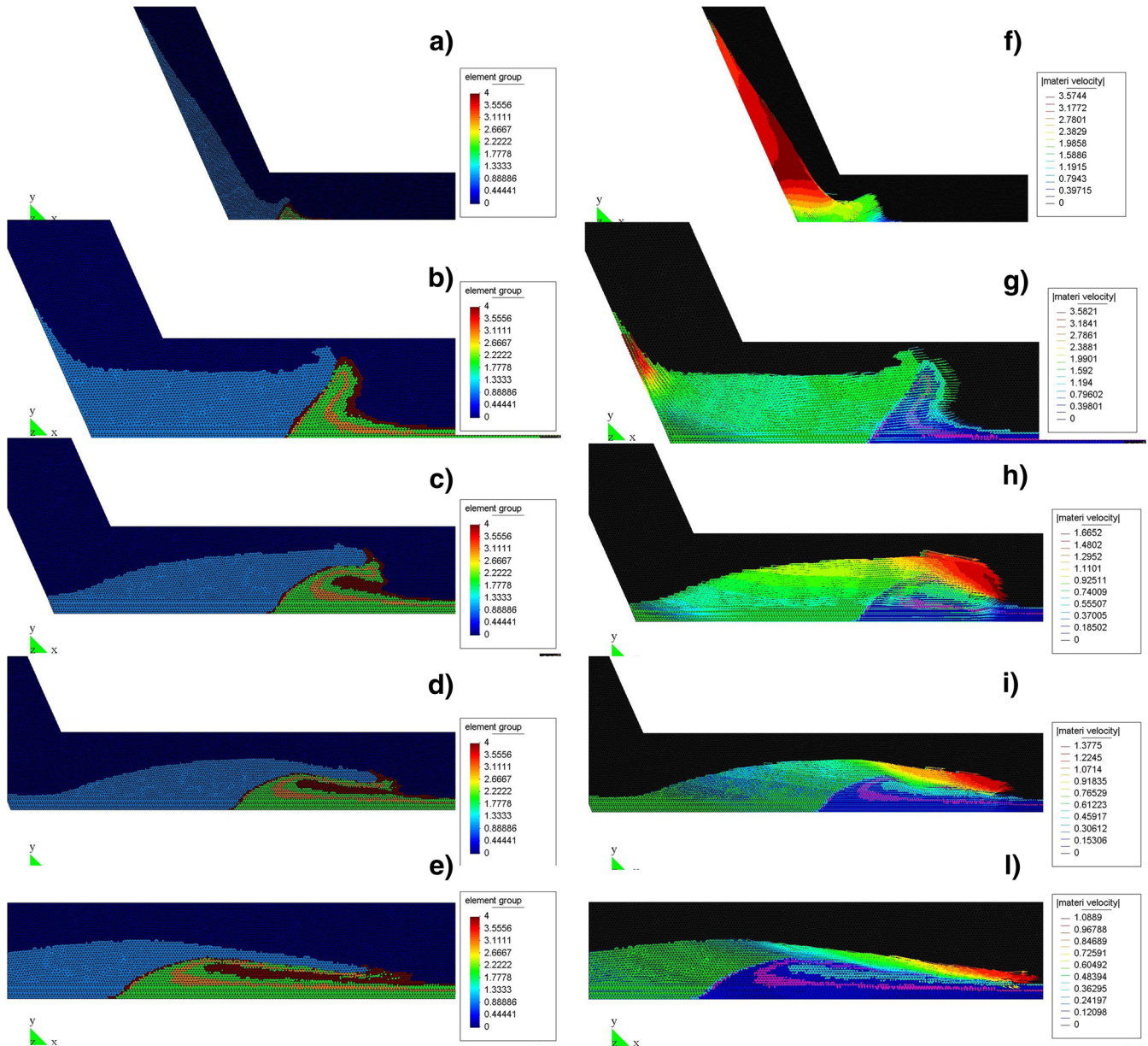


Fig. 17 2D FEM simulation of the test with layered sand layers as in Fig. 7. Orange layer as in Fig. 7, whereas brown layer corresponds to blue layer in Fig. 7. Material distribution (a–e) and velocity vectors (f–l) for a FEM plane strain simulation for geometrical conditions (Fig. 2, for $\theta = 66^\circ$) and physical mechanical properties (Table 1) as in the experimental tests. Legend for velocity vectors is rescaled at each time step. Layered erodible material is represented on the *horizontal plane*. Final front inclination: ca 11°

snout at the front and an elongating tail. The final deposit has a lobate geometry with a gentler frontal slope with respect to the upward side (Fig. 16).

In this case, the final deposit geometry fits well with the experimental results (Figs. 16 and 17c, 50°), with a maximum thickness of 8 cm and runout of 110 cm from the upper release limit compared to the experimental values of ca. 7.5 and 115 cm. Impact at the slope base occurs between 0.6 and 0.7 s (Fig. 17), with the maximum front velocity of about $2.7\text{--}2.9\text{ m s}^{-1}$. At 0.7 s, the avalanche material undergoes a change in direction with velocity vectors pointing downstream and upward, and the erodible layer is set in motion. At 0.9 s, the steep front of the flow runs at high

speed. The evolution of the material front during the experiment is reported in Fig. 2b, where the position of the front is reported both for the eroded material and the falling mass. These data can be compared to those of the laboratory experiment (50° , 5.1 l) in the same figure (Figs. 18 and 19).

3D simulations show the spreading of the flowing mass along the slope as well as the distribution of erosion and deposition (see also Fig. 16). To better investigate the avalanche geometry at and after the impact, the erosion process, and the internal deformation of the erodible basal layer, a 2D modeling approach is more suitable mainly due to the lower computational requirements. At the same time, with these simulations, it is possible to test the

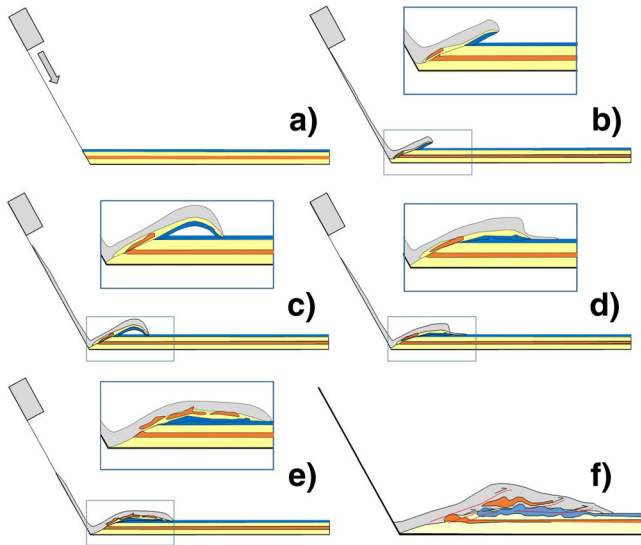


Fig. 18 Internal structures and kinematic interpretation of the erosion and deposition from the result of the experiments with colored sand layers. a–e Sketches of the evolution of the colored layers and of the flow surface at different time steps. f Final distribution of the colored layers within the deposit (compare Figs. 7e and 17f). For phases b–e, enlargements of the sector (within the rectangular box) affected by erosion are shown

validity of using a continuous elasto-plastic modeling approach for modeling the erosion and deposition phase both at the laboratory and eventually at larger scales. The 2D simulations (Figs. 16 and 17) clearly show the generation of a steep front and the jump of the avalanche flow above the basal layer. The basal layer is completely pushed away at the front of the avalanche and starts to be eroded from the surface and folded at depth (Fig. 17a). In Fig. 17f, the decreasing velocity of the material climbing at the front and eroding the layer can be observed, as well as the high

velocity of the material still rushing down the slope and pushing the front from the rear. The maximum velocity at impact is about $3.2\text{--}3.5\text{ m s}^{-1}$ (see Fig. 17f–l) and comparable to the one computed (Eq. 7) assuming a basal friction angle of 25° (3.57 m s^{-1}) and 31° (3.44 m s^{-1}). The upper part of the front starts climbing up against the basal sandy material, along a steep and straight shear band, and overpasses the crest generated in the basal layer. The dragging and pushing of the material continues (Fig. 17b) with the front part composed of the basal material becoming progressively steeper, until an overturn fold starts developing. The front of the avalanche material, slowed by the folding basal layer, collapses backward (Fig. 17g). The fold is completely overturned, and the upstream (left hand limb) is torn off, with a thin discontinuous layer of orange and brown sand remaining below the avalanche ramp (Fig. 17c), and the shear plane below the avalanche assumes an S-shaped geometry. At this step, the brown layer is completely overturned and doubled in thickness. The velocity vectors (Fig. 17h) suggest at this time a sort of front instability. The final two steps (Fig. 17d, e) are characterized by the elongation of the deposit (see also Fig. 17i, l) and of the S-shaped contact band between the avalanche material and the overturned basal layer. The final front inclination at 21° is compatible with the 22° for the experimental test (see Fig. 16c). It is worth noting that because of the plane strain conditions, the flow reaches the slope toe with a thickness greater than the measured one. As a consequence, the simulated avalanche erodes away a longer part of the basal layer compared to experimental data. Nevertheless, this set of observations fits fairly well to the experimental ones (see Figs. 7, 17e, and 16c).

Discussion

There are numerous cases of landslides (Fig. 1 and Table S1 in Supporting Information) and granular flows occurring along a steep slope followed by a sub-horizontal and planar spreading

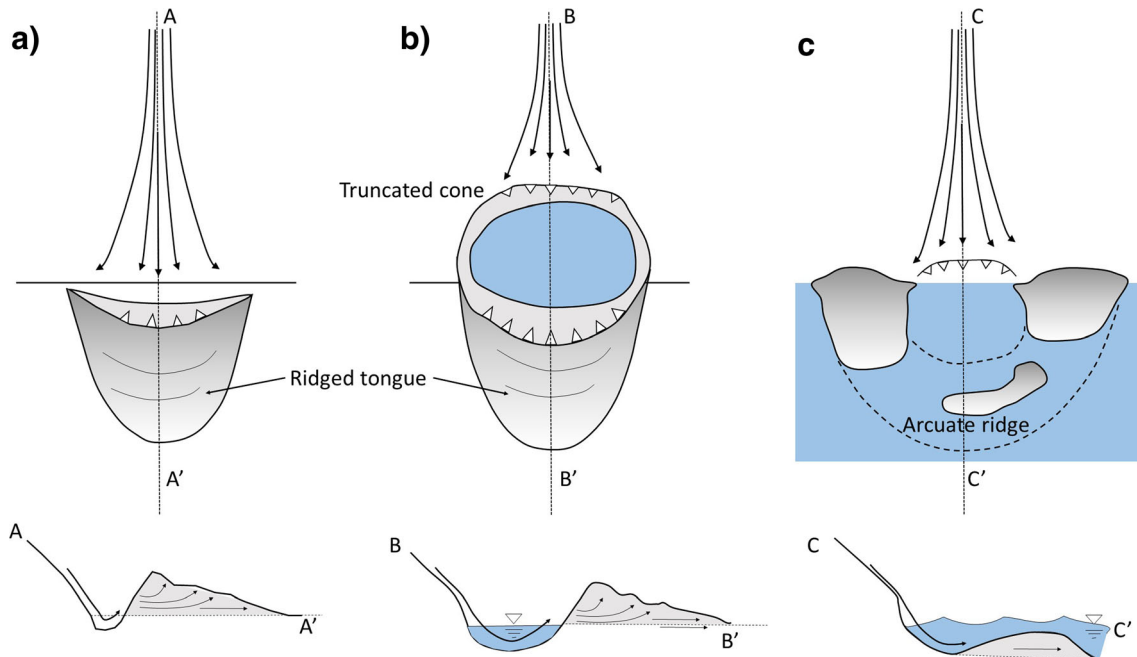


Fig. 19 Three typologies of snow avalanche impact depressions in the Troms area of Norway according to Corner (1980). For each variety, the upper figure shows the scheme of formation, and the lower diagram an ideal cross-section. a Tongue-like. b Pit. c Pool. In some cases, water fills up the depression (blue). From Corner (1980), modified

area. Flat areas often coincide with an alluvial plain made of an erodible substrate.

Runout

Hutchinson (2002) and Duperré et al. (2006) describe collapses of chalk headwalls (see data in Table S1) onto flat tidal areas in northern Europe. Recognizing that vertical collapses exhibit shorter runouts than those occurring along a gentler slope, Hutchinson (2002) suggests that this is because vertical collapses involve harder and less porous rocks, less prone to water remolding and loss of strength. However, he also points out that a vertical collapse has a smaller horizontal component of the initial velocity. Table S1 and Fig. 14 report data for rock avalanches with steep slopes and show an increasing trend of H/L with slope angle, as noticed in experiments with large cubic blocks (Okura et al. 2000, 2003). Figure 13a shows the increasing trend with slope angle and with the thickness of the erodible layer, with minimal H/L values for a perfectly smooth and sand-free surface (stars), and an opposite trend is recognized with respect to the released volume. Figure 13b, c shows the H/L relationship with the sand layer thickness as a function of the type and volume of released material. They show a sort of saturation effect for thicker layers (2 cm), with a stabilization of the H/L value, suggesting that the flow erosivity cannot remove the entire thickness of the basal layer.

Figure 14 shows the results of the experiments and rock avalanche/flowslide data (Table S1) on the same plot. Rock avalanches fall in the lowermost region of the graph. Data describing the nearly vertical collapse of large masses in the Yosemite valley (see Table S1, Wicczorek et al. 1999; Stock and Uhrhammer 2010) and chalk cliff collapses (Hutchinson 2002; Duperré et al. 2006) exhibit a much higher value of H/L . Data of our experiments fall in the region between these two data sets, above the real large rock avalanches and to the left of vertical cliff collapses. At the same time, many rock avalanche deposits of small to medium size show a behavior similar to that of the experiments. We suggest a continuity in behavior and, despite the difference in scale, a similarity between these different granular flows.

Figure 9a also shows the prediction of the simple model of Eq. 3. This model can explain the increase in H/L with the slope, even though different parameters should be adopted for the three different data sets. Real data can be fitted with relatively low friction coefficient and a coefficient of restitution of the order 0.2–0.3. With such values, both data sets for rock avalanches and chalk flows are approximately fitted by one single curve. This implies that the sharp increase in H/L for nearly vertical collapses could be predicted by this simple analysis without invoking any anomalous behavior of the chalk (Hutchinson 2002). Experimental data, however, require higher values of the friction coefficient, like the one measured in the laboratory. In our model, the length L in the ratio H/L is calculated as the sum of the horizontal slope on the inclined plate, plus the length on the horizontal plate due to the residual horizontal velocity at the slope break. Our analysis with zero coefficient of restitution is compatible with Okura's model (Okura et al. 2000) for total loss of the vertical kinetic energy component at the slope break.

The plot in Fig. 9a also shows an empirical correlation between the length of the deposit at the slope foot and the total length of the granular flow. Here, following a modified version of the $\alpha\beta$ -

model by Lied and Bakkehøi (1980) for snow avalanches, we seek a correlation between the angle of slope θ and the angle of *Fahrboschung* $\alpha = \tan^{-1}(H/L)$ in the form $\alpha = K\theta + B$, where K and B are fitting constants. This empirical formula, shown in Fig. 9 with a dashed line ($H/L = \tan \alpha = 0.618\theta + 9.8$), appears to roughly fit our data. The fact that the fitting coefficients for the experiments are much different from those pertinent to snow avalanches (0.77–0.94 instead of 0.618; McClung 2001) is not surprising considering the complexity of snow avalanches in terms of wetting, cohesion, and air entrainment. However, the analysis shows that the increase of H/L with slope angle has a common origin. Comparison with the analysis by Lucas et al. (2014) shows that we need a very large value of the constant k to fit the H/L dataset, adopting their equation for Heim's ratio.

We note that the results of Fig. 9 could also be applicable to the well-known problem of the volume effect, i.e., the decrease of the ratio H/L (Scheidegger 1973) and of the effective friction coefficient ($\mu_{\text{eff}} = \tan\theta + H_0/\Delta L$ where ΔL is the total runout measured along the real path; Lucas et al. 2014) as a function of the volume for large rock avalanches. Although many theories have been put forward to explain the volume effect (e.g., Legros 2002; De Blasio 2011b for short reviews; Lucas et al. 2014), the fact that larger landslides will have lower impact angle θ shows that at least part of the reason for the volume effect could be geometrical.

Dynamics

There are obvious differences between the different sets of laboratory and field data of Fig. 9. Our experimental flows are dry, while chalk collapses occur in a wet environment; rock avalanches are mostly dry, but a collapse onto an alluvial plain can lubricate their basal layers. Other experiments on an inclined granular bed, with no sharp break in slope, have shown a gain rather than loss of mobility when the flume gradient is steeper than approximately half the angle of repose of the material (Mangeney et al. 2010; Farin et al. 2014). This might be explained by the fact that the inclination causes an increase of the shear stress, and a dry granular medium at slopes close to the angle of repose (or to critical friction angle; Crosta et al. 2015a) is highly unstable. For wet materials close to saturation, the effect might be more dramatic with increased erosion and entrainment, and feedback effects leading in principle to unbounded growth of the flowing material (Breien et al. 2008; De Blasio et al. 2011; Iverson et al. 2011). Another difference is the effect of fragmentation of the granular mass, which is absent in the experiments given the fine grain size and low impact energy, but might alter the propagation of a real rock avalanche (McSaveney and Davies 2007; Bowman et al. 2012) especially in correspondence to an abrupt break of slope (Crosta et al. 2007; De Blasio and Crosta 2014; 2015a). Considering these differences, the continuity between data and experimental flows is encouraging (Fig. 14).

Summarizing all the tests, a sequence of mechanisms occurring during the flow and deposition is suggested. As soon as the material impacts against the erodible substrate at the slope break, a sort of reflection controlled by the descent angle causes the ballistic/quasi ballistic projection of the material. The basal layer is dilated and eroded, and steeper deposit accumulates at the downstream side from which grains are launched ballistically. Where the ballistic trajectories meet the ground horizontal surface, a type of breaking wave is generated (Fig. 8b, c), which steepens

during the earlier stages to become progressively gentler. During these stages, the flow and the wave erode material and transport it downstream causing a double (multiple) layering of the originally static material (tests with colored sand layers, Fig. 7).

Another interesting feature observed in the experiments for steep to very steep slopes ($>45^\circ$) and in the numerical simulations (Crosta et al. 2015a, b and Fig. 5c) is the presence of a depression or groove left behind the deposit at the base of the inclined slope (for gentle slopes, a backward propagating shock wave covers the slope toe, and no depression is formed). Similar features have been described at the cliff foot for chalk falls (Hutchinson 2002) or for snow avalanches from steep slopes (Corner 1980; Smith et al. 1994; Fitzharris and Owens 1984). Figure 10 shows a scheme of the morphology of snow-generated hollows. The impact pit geometry for snow avalanches (Smith et al. 1994; Owen et al. 2006) suggests the role of impact force and erosion exerted by the highly energetic flow at reshaping the slope toe. Both the truncated cone (B) and lunate ridge (B) created by snow avalanches in the natural setting resemble structures observed in the experiments and in the simulations. We suggest that the depression observed in the numerical simulation at the slope break is a good model for the pits observed in the field and in the experiments.

The upstream shock wave propagation is evident together with the infilling of the upstream depression which initially isolates the crest of the deposit. This depositional process causes a progressive upstream displacement of the center of mass at increasing the deposited volume. Experiments using a coarse angular gravel (Figs. 6 and 8c) confirm the role of the flowing mass on the erosion of the basal layer and the rapid mobilization of material with a type of ballistic motion. In this case, the eroded sand generates a wave running below the coarse gravel, which floats and finally stops on the top of the sand deposit. Noticeably, the total runout, under the same experimental conditions, is longer for the case of sand on sand experiments. All these observations suggest that the thin layer approximation with minimal internal shear does not fit the evolution described here. Dense shear flow conditions, the formation of ramp-like structures, and the full detachment of the flow front with formation of a breaking front are highly dynamic features.

As a further comparison with the field data, we consider the Savage's number (Savage 1984) which gives the ratio between inertial to gravity forces during the movement of the granular medium

$$N_{SAV} = D \frac{\dot{\gamma}^2}{g}$$

where D is the grain diameter and $\dot{\gamma}$ is the shear rate. Our experimental Savage's number estimated during the collapse phase onto the horizontal board is typically of the order 10^{-2} , which indicates a prevalence of gravity over inertia. The ratio between the Savage's number for the field and the experiments can be recast in the form

$$\frac{N_{SAV}(\text{field})}{N_{SAV}(\text{exp})} = \frac{D(\text{field})}{D(\text{exp})} \frac{H(\text{field})}{H(\text{exp})} \left(\frac{T(\text{exp})}{T(\text{field})} \right)^2$$

where D , H , and T are respectively the grain size, the fall height, and the thickness of the shear layer. Except for the fall height H (which is, however, extremely variable between different

landslides), D and T are poorly known and are also likely to vary enormously in the field. Using indicative ratios $\frac{D(\text{field})}{D(\text{exp})} = 1$ to 10 0; $\frac{H(\text{field})}{H(\text{exp})} = 1000$; $\frac{T(\text{exp})}{T(\text{field})} = 1/100$ it is estimated that $\frac{N_{SAV}(\text{field})}{N_{SAV}(\text{exp})}$ may vary between 0.1 and 10. Thus, the experimental apparatus falls within the limit values of typical Savage's numbers occurring in nature.

All these observations suggest that the thin layer approximation with minimal internal shear does not fit the evolution described here, and multi layer models would be more realistic in the modeling of the real evolution. Dense shear flow conditions, the formation of ramp-like structures, and the full detachment of the flow front with formation of a breaking front are highly dynamic features. This also supports the adoption of fully continuum or DEM models. Even if a simple elasto-plastic law does not allow an exact modeling of the entire phenomenon, it succeeds at providing a qualitatively good geometrical fitting and especially at describing the internal deformation to which the material is subjected.

Conclusions

This paper presents the results of a series of physical and numerical experiments where a granular mass released along a slope reaches a horizontal plate with an abrupt slope change. If the horizontal plate is devoid of any granular material, the presence of a break of slope in the topography affects both dynamics and runout. The geometry of the break of slope causes a loss of momentum perpendicular to the basal layer, with longer runout when the slope break is smoothed. Our observations substantiate and extend those made by Rowley et al. (2011) to a broader set of conditions (different slope angles and materials) by a detailed description of the evolution with time, and of the erosion mechanisms.

The main novelty of the present work, however, has been the study of the interaction of the granular flow descending along the slope with an erodible substrate of sand resting on the horizontal plate. To observe the dynamics of erosion and entrainment, the time evolution of the flow was monitored in detail. The modes of accretion and the final geometry of the deposit are found to be closely associated with the slope angle and the momentum of the flow. In general, the presence of a dry erodible substrate was found to hinder the further flow of the granular mass, but increase its volume. Thus, the experiments suggest that in a real landslide, a granular flow falling at a steep angle onto a loose, dry erodible substrate will decrease its speed and runout. The physical reason for this lays in the transfer of momentum to the erodible substrate.

A series of analytical and numerical models are presented to simulate experimental tests. A solution for the H/L ratio which contains the effect of the abrupt slope break and a coefficient of restitution is presented, and the obtained relationship fits well both the experiments and the real case data.

Numerical simulations via a FEM ALE approach, adopting an elasto-plastic Mohr Coulomb material description, confirm the direct increase on the runout when the slope break is smoothed. The dynamics of flow, erosion, and entrainment simulated numerically supports the observation of a dense flow condition especially during the propagation along the horizontal portion and the internal shearing until the final deposition. The numerical results reproduce well the dynamics observed, peak velocity and total duration, including the dense shear flow erosion of the basal layer and the geometry of the final deposit. Starting from recent modeling literature, the adoption of a $\mu(I)$ frictional rheology is

suggested for modeling this type of processes. Future efforts will test a visco-plastic approach on the same set of data and constraints.

Acknowledgments

The data for this paper are available upon request from the authors. The research was supported by PRIN Project: time-space prediction of high impact landslides under changing precipitation regimes PRIN 2010–2011—prot. 2010E89BPY_007 project by the Italian Ministry of Research and University. Jeff Warburton is thanked for the critical reviewing of an early version of the manuscript.

Appendix

References

- ASTM D3080 / D3080M-11 (2011) Standard Test Method for Direct Shear Test of Soils Under Consolidated Drained Conditions, ASTM International, West Conshohocken, PA, 2011, www.astm.org
- ASTM D7263-09 (2009) Standard test methods for laboratory determination of density (unit weight) of soil specimens, ASTM International, West Conshohocken, PA, 2009, www.astm.org
- Bowman ET, Take WA, Rait KL, Hann C (2012) Physical models of rock avalanche spreading behaviour with dynamic fragmentation. *Can Geotech J* 49:460–476
- Breien H, De Blasio FV, Elverhøi A, Hoeg K (2008) Erosion and morphology of a debris flow caused by a glacial lake outburst flood. *Landslides*. doi:10.1007/s10346-008-0118-3
- Calvetti F, Crosta G, Tatarella M (2000) Numerical simulation of dry granular flows: from the reproduction of small-scale experiments to the prediction of rock avalanches. *Rivista Italiana di Geotecnica* 34(2):21–38
- Chen H, Crosta GB, Lee CF (2006) Erosional effects on runout of fast landslides, debris flows and avalanches: a numerical investigation. *Geotechnique* 56(5):305–322

Table 3 List of the mathematical symbols used in this work and their meaning

Symbol	Meaning
B	Height of the granular flow in the release box
D	Thickness of the granular flow
D'	Thickness of the eroded layer
D_{MAX}	Maximum erodible thickness
f	Fraction of the velocity of one ballistic grain with respect to the initial velocity in the problem of ballistic jump (Eq. 13)
f_{CRIT}	Critical value of f
g	Gravity acceleration
H	Fall Height of the granular flow (or landslide)
H/L	Fahrboeschung
L	Runout of the granular flow (or landslide)
L'	Length of the sloping board
M	Mass of the granular flow
M'	Mass of the eroded material
R_H	Runout on the horizontal table without erosion
R_H^*	Runout on the horizontal table with erosion
S	Basal surface area of the granular flow
U_x	Horizontal velocity past the slope break
u_{entr}	Velocity of the granular flow after entrainment
u_o	Horizontal velocity at the slope break
X	Maximum horizontal distance of a grain in ballistic flight
x	Horizontal distance of the granular flow (meant as a variable)
δ	Angle of attack of the deposit in the evaluation of the
ΔL	Total runout measured along the real path
ε	Coefficient of restitution
μ	Friction coefficient
μ_{eff}	Effective friction coefficient (accounting also for the initial height of the granular material)
ρ	Density of granular flow
θ	Inclination angle of the board

- Choffat P (1929) L'écroulement d'Arvel (Villeneuve) de 1922. *Bull Soc Vaudoise Sci Nat* 57(1):5–28
- Corner GD (1980) Avalanche impact landforms in Troms, North Norway. *Geogr Ann* 62A:1–10
- Crosta G (1992) An example of unusual complex landslide: from a rockfall to a dry granular flow? 2nd Conv. Giovani Ricercatori di Geologia Applicata, 27–31 October 1992, Viterbo, *Geologica Romana*, Roma, vol 30, 175–184
- Crosta GB, Imposimato S, Roddeman D, Chiesa S, Moia F (2005) Small fast moving flow-like landslides in volcanic deposits: the 2001 Las Colinas Landslide (El Salvador). *Eng Geol* 79(3–4):185–214. doi:10.1016/j.enggeo.2005.01.014
- Crosta GB, Imposimato S, Roddeman DG (2006) Continuum numerical modelling of flow-like landslides. In: Evans SG, Scarascia Mugnozza G, Strom A, Hermanns R (eds) *Landslides from massive rock slope failure*. NATO science series. Earth Environ Sci, vol 49. Springer, Dordrecht, pp 211–232
- Crosta GB, Frattini P, Fusi N (2007) Fragmentation in the Val Pola rock avalanche. *Italian Alps J Geophys Res* 112:F01006. doi:10.1029/2005JF000455
- Crosta GB, Imposimato S, Roddeman D (2008) Numerical modelling of entrainment/deposition in rock and debris-avalanches. *Eng Geol* 109(1–2):135–145
- Crosta GB, Imposimato S, Roddeman D (2009) Numerical modeling of 2-D granular step collapse on erodible and non erodible surface. *J Geophys Res* 114:F03020
- Crosta GB, Imposimato S, Roddeman D (2013a) Interaction of landslide mass and water resulting in impulse waves. In: Margottini C, Canuti P, Sassa K (eds) *Landslide science and practice*, vol 5: Complex Environment. Springer, Berlin Heidelberg, pp 49–56. doi:10.1007/978-3-642-31427-8
- Crosta GB, Imposimato S, Roddeman D, Frattini P (2013b) On controls of flow-like landslide evolution by an erodible layer. In: Margottini C, Canuti P, Sassa K (eds) *Landslide science and practice*, vol 3: Spatial Analysis and Modelling. Springer, Berlin Heidelberg, pp 263–270. doi:10.1007/978-3-642-31427-8
- Crosta GB, Imposimato S, Roddeman D (2015a) Granular flows on erodible and non erodible inclines. *Granul Matter*. doi:10.1007/s10035-015-0587-8
- Crosta GB, Imposimato S, Roddeman D (2015b) Landslide spreading, impulse water waves and modelling of the Vajont Rockslide. *Rock Mech Rock Eng* 1–24. doi:10.1007/s00603-015-0769-z
- Cruden DM, Hungr O (1986) The debris of Frank slide and theories of rockslide-avalanche mobility. *Can J Earth Sci* 23:425–432
- De Blasio FV (2011a) Landslides in Valles Marineris (Mars): a possible role of basal lubrication by sub-surface ice. *Planet Space Sci* 59:1384–1392. doi:10.1016/j.pss.2011.04.015
- De Blasio FV (2011b) Introduction to the physics of landslides. Springer Verlag, Berlin (420 pp)
- De Blasio FV, Crosta GB (2014) Simple physical model for the fragmentation of rock avalanches. *Acta Mech*. doi:10.1007/s00707-013-0942-y
- De Blasio FV, Breien H, Elverhøi E (2011) Modelling a cohesive-frictional debris flow: an experimental, theoretical, and field-based study. *Earth Surf Process Landf* 36:753–766
- Denlinger RP, Iverson RM (2001) Flow of variably fluidized granular masses across three-dimensional terrain: 2. Numerical predictions and experimental tests. *J Geophys Res* 106(B1):553–566. doi:10.1029/2000JB900330
- Dufresne A (2012) Granular flow experiments on the interaction with stationary runout path materials and comparison to rock avalanche events. *Earth Surf Process Landf* 37:1527–1541
- Duperret A, Genter A, Martinez A, Mortimore RN (2006) Coastal chalk cliff instability in NW France: role of lithology, fracture pattern and rainfall. In: Mortimore RN, Duperret A (eds) *Coastal chalk cliff instability*, vol 20. Geological Society, London, Engineering Geology Special Publications, The Geological Society of London, London, pp 33–55
- Erismann TH, Abele G (2001) Dynamics of rockslides and rockfalls. Springer, Berlin, 316 pp
- Farin M, Mangeney A, Roche O (2014) Fundamental changes of granular flow dynamics, deposition and erosion processes at high slope angles: insights from laboratory experiments. *J Geophys Res Earth Surf* 119:504–532. doi:10.1002/2013JF002750
- Fitzharris BB, Owens IF (1984) Avalanche tarns. *J Glaciol* 30(106):308–312
- Forterre Y, Pouliquen O (2008) Flows of dense granular media. *Annu Rev Fluid Mech* 40:1–24
- Gray JMNT, Wieland M, Hutter K (1999) Gravity-driven free surface flow of granular avalanches over complex basal topography. *Proc R Soc Lond A* 455:1841–1874. doi:10.1098/rspa.1999.0383
- Hakonardottir KM, Hogg AJ, Johannesson T, Tomasson GG (2003a) Large scale avalanche braking mound and catching dam experiments with snow. A study of the airborne jet. *Surv Geophys* 24:543–554
- Hakonardottir KM, Hogg AJ, Johannesson T, Tomasson GG (2003b) A laboratory study of the retarding effects of braking mounds on snow avalanches. *J Glaucoma* 49(165):191–200
- Heim A (1882) Der Bergsturz von Elm. *DeutschGeol Gesell Zeitschr* 34:74–115
- Heim A (1932) Bergsturz und Menschenleben. Fretz und Wasmuth, Zürich, 218 pp
- Hewitt K et al (2006) Rock avalanches with complex run out and emplacement, Karakoram Himalaya, Inner Asia. In: Evans SG (ed) *Landslides from Massive Rock Slope Failure*. Springer, Printed in the Netherlands, pp 521–550
- Hsu K (1975) Catastrophic debris streams (Sturzstroms) generated by rockfalls. *Geol Soc Am Bull* 86:129–140
- Hutchinson JN (2002) Chalk flows from the coastal cliffs of northwest Europe. *Geol Soc Am Rev Eng Geol* 2002(15):257–302
- Iverson RM (2012) Elementary theory of bed-sediment entrainment by debris flows and avalanches. *J Geophys Res* 117:F03006. doi:10.1029/2011JF002189
- Iverson RM, Ouyang C (2015) Entrainment of bed material by Earth-surface mass flows: review and reformulation of depth-integrated theory. *Rev Geophys* 53:27–58. doi:10.1002/2013RG000447
- Iverson RM, Reid ME, Logan M, LaHusen RG, Godt JW, Griswold JG (2011) Positive feedback and momentum growth during debris-flow entrainment of wet bed sediment. *Nat Geosci* 4:116–121. doi:10.1038/NGEO1040
- Jaboyedoff M (2003) The rockslide of Arvel caused by human activity (Villeneuve, Switzerland): summary, partial reinterpretation and comments of the work of Ph. Choffat (1929): L'écroulement d'Arvel (Villeneuve) de 1922. *Bull. SVSN* 57, 5 – 28, Open File Rep. 3, Int. Indep. Cent. of Clim. Change Impact on Nat. Risk Anal. in Mt. Areas, Lausanne, Switzerland. http://www.quanterra.org/erosion_hazard.htm last accessed 28 March 201
- Lacaze L, Phillips JC, Kerswell RR (2008) Planar collapse of a granular column: experiments and discrete element simulations. *Phys Fluids* 20:063302.1–063302.12. doi:10.1063/1.2929375
- Lajeunesse E, Mangeney-Castelnau A, Vilotte JP (2004) Spreading of a granular mass on a horizontal plane. *Phys Fluids* 16:2371–2381. doi:10.1063/1.1736611
- Lajeunesse E, Monnier JB, Homsy GM (2005) Granular slumping on a horizontal surface. *Phys Fluids* 17:103302.1–103302.15. doi:10.1063/1.2087687
- Legros F (2002) The mobility of long-runout landslides. *Eng Geol* 63:301–331
- Lied K, Bakkehoi S (1980) Empirical calculations of snow-avalanche run-out distance based on topographic parameters. *J Glaucoma* 26:165–177
- Lube G, Huppert H, Sparks S, Freundt A (2005) Collapses of two dimensional granular columns. *Phys Rev E* 72:041301.1–041301.10. doi:10.1103/PhysRevE.72.041301
- Lucas A, Mangeney A, Ampuero JP (2014) Frictional velocity-weakening in landslides on Earth and on other planetary bodies. *Nat Commun* 5:3417, DOI: 10.1038
- Lucchitta BK (1979) Landslides in Valles Marineris, Mars. *J Geophys Res* 84(B14):8097–8113. doi:10.1029/JB084B14p08097
- Ma A, Liao H, Ning C, Feng Z (2014) Stability analysis of a high slope along a loess plateau based on field investigation and numerical analysis. In: Sassa K et al (eds) *Landslide science for a safer geoenvironment*, vol 1. Springer, Berlin Heidelberg, pp 451–458
- Mangeney A, Tsimring LS, Volfson D, Aranson IS, Bouchut B (2007) Avalanche mobility induced by the presence of an erodible bed and associated entrainment. *Geophys Res Lett* 34:L22401
- Mangeney A, Roche O, Hungr O, Mangold N, Faccanoni G, Lucas A (2010) Erosion and mobility in granular collapse over sloping beds. *J Geophys Res* 115:F03040. doi:10.1029/2009JF001462
- Manzella I, Labiouse V (2008) Qualitative analysis of rock avalanches propagation by means of physical modelling of not constrained gravel flows. *Rock Mech Rock Eng* 41(1):133–151
- Manzella I, Labiouse V (2013) Empirical and analytical analyses of laboratory granular flows to investigate rock avalanche propagation. *Landslides* 10:23–36. doi:10.1007/s10346-011-0313-5
- McClung DM (2001) Extreme avalanche runout: a comparison of empirical models. *Can Geotech J* 38:1254–1265. doi:10.1139/cgj-38-6-1254
- McConnell RG, Brock RW (1904) Report on great landslide at Frank, Alberta, Canada. Can. Dept. Inter. Annual Rep., 1902—1903, Part 8, 17 pp
- McSaveney MJ, Davies T (2007) Rockslides and their motion. In: Sassa K, Fukuoka F, Wang F, Wang G (eds) *Progress in landslide science*. Springer, Berlin, pp 113–133
- McSaveney MJ, Davies TRH, Hodgson KA (2000) A contrast in deposit style and process between large and small rock avalanches. In: Bromhead E, Dixon D, Ibsen M–L, Bromhead E, Dixon D, Ibsen M–L (eds) *Landslides in research, theory and practice*. Thomas Telford Publishing, London, pp 1053–1058

- Okura Y, Kitahara H, Sammori T, Kawanami A (2000) The effects of rockfall volume on runout distance. *Eng Geol* 58(2):109–124
- Okura Y, Kitahara H, Kawanami A, Kurokawa U (2003) Topography and volume effects on travel distance of surface failure. *Eng Geol* 67:243–254
- Owen G, Matthews JA, Shakesby RA, He X (2006) Snow-avalanche impact landforms, deposits and effects at Urdvatnet, Southern Norway: implications for avalanche style and process. *Geografiska Annaler: Ser A Phys Geogr* 88:295–307. doi:10.1111/j.0435-3676.2006.00302.x
- Pastor M, Blanc T, Pastor MJ (2009) A depth-integrated viscoplastic model for dilatant saturated cohesive-frictional fluidized mixtures: application to fast catastrophic landslides. *J Non-Newtonian Fluid Mech* 158:142–153
- Pastor M, Blanc T, Haddad B, Petrone S, Morles MS, Drempetic V, Issler D, Crosta GB, Cascini L, Sorbino G, Cuomo S (2014) Application of a SPH depth-integrated model to landslide run-out analysis. *Landslides* 11(5):793–812. doi:10.1007/s10346-014-0484-y
- Pudasaini SP, Hutter K (2006) *Avalanche dynamics: dynamics of rapid flows of dense granular avalanches*. Springer, Berlin Heidelberg, 602 pp
- Pudasaini S, Kroner C (2008) Shock waves in rapid flows of dense granular materials: theoretical predictions and experimental results. *Phys Rev E* 78:041308
- Roddeман DG (2008) TOCHNOG user's manual. FEAT, 255 pp, www.feat.nl/manuals/user/user.html
- Rowley PJ, Kokelaar P, Menzies M, Waltham D (2011) Shear-derived mixing in dense granular flows. *J Sediment Res* 81:874–884. doi:10.2110/jsr.2011.72
- Savage SB (1984) The mechanics of rapid granular flows. *Adv Appl Mech* 24:289–366
- Scheidegger AE (1973) On the prediction of the reach and velocity of catastrophic landslides. *Rock Mech* 5:231–236
- Smith DJ, McCarthy DP, Luckman BH (1994) Snow-avalanche impact pools in the Canadian Rocky Mountains. *Arct Alp Res* 26(2):116–127
- Staron L (2008) Mobility of long-runout rock flows: a discrete numerical investigation. *Geophys J Int* 172(1):455–463
- Stock GM, Uhrhammer RA (2010) Catastrophic rock avalanche 3600 years BP from El Capitan, Yosemite Valley. *Calif Earth Surf Process Landf* 35:941–951. doi:10.1002/esp.1982
- Strom A (2006) Morphology and internal structure of rockslides and rock avalanches: grounds and constraints for their modelling. In: Evans SG, Scarascia Mugnozza G, Strom A, Hermanns R (eds) *Landslides from massive rock slope failure*. NATO Science Series. Earth Environ Sci, vol 49. Springer, Dordrecht, pp 305–326
- Taboada A, Estrada N (2009) Rock-and-soil avalanches: theory and simulation. *J Geophys Res* 114:F03004. doi:10.1029/2008JF001072
- Uttili S, Zhao T, Houlsby GT (2015) 3D DEM investigation of granular column collapse: evaluation of debris motion and its destructive power. *Eng Geol* 186:3–16
- von Poschinger A, Kippel T (2009) Alluvial deposits liquefied by the Flims rock slide. *Eng Geol* 103(1):50–56
- Wieczorek GF, Morrissey MM, Iovine G, Godt J (1999) Rock-fall potential in the Yosemite Valley, California: U.S. Geological Survey Open File Report 99–578, 1 plate, scale 1:12 000, 7. <http://greenwood.cr.usgs.gov/pub/open-file-reports/ofr-99-0578/> last accessed 28 March 2016
- Zhao T, Uttili S, Crosta GB (2015) Rockslide and impulse wave modelling in the Vajont reservoir by DEM-CFD analyses. *Rock Mech Rock Eng* 1–20. doi:10.1007/s00603-015-0731-0

Electronic supplementary material The online version of this article (doi:10.1007/s10346-016-0697-3) contains supplementary material, which is available to authorized users.

G. B. Crosta (✉) · **F. V. Blasio** · **M. Caro** · **G. Volpi**

Department of Earth and Environmental Sciences,
Università degli Studi di Milano Bicocca,
Milan, Italy
e-mail: giovannibattista.crosta@unimib.it

S. Imposimato · **D. Roddeман**

FEAT,
Heerlen, The Netherlands